0.5T Benchtop Magnet:

Development of a MR Elastography Setup

and Tissue Samples Characterization

BY

MARCO ANDREA ZAMPINI
B.S, Politecnico di Milano, Milan, Italy, 2016

THESIS

Submitted as partial fulfillment of the requirements
for the degree of Master of Science in Bioengineering
in the Graduate College of the
University of Illinois at Chicago, 2018

Chicago, Illinois

Defense Committee:

Dieter Klatt, Chair and Advisor
Richard Magin
Guido Baroni, Politecnico di Milano

ACKNOWLEDGMENTS

I would like to express my gratitude to Dr. Dieter Klatt for his guidance, the help I received and the trust I was given throughout this project. All the Motion-Encoding MRI Laboratory and Dr. Braun from Charité University are acknowledged for the comments, suggestions and practical support.

Many thanks to Dr. Richard Magin for his helpfulness and valuable insights on the MRI world. I found out you were right when you told me that this topic is like an onion, with layer after layer and tears involved in each of them.

Chiara Paganelli and Giulia Buizza: thanks for the backing and the commitment you provided me since I started my experience in Chicago.

To my flat mates Greta, Elena, Martina and Leonardo goes my deep appreciation for making me feel the homesickness a little less and for being my home away from home. Thanks for the "acqua calda", for the room in the fridge and allowing my food invasion over Greta's shelf, for tons of risotti and never ending BBQ sauce, for Mr Pollo & Mr Salmon, for musicals and Sense8 binge watching and many other wonderful memories. All the Polimi group: thanks for the laughters and this time spent together in this multi-colored city.

Martina (Gina): thanks for the real help and support, let's say it was just essential. Your name should be on the dictionary as an exemplification of "survival guide".

Also, I have to mention Annalisa, Laura, Rosti and Vlad. You were fundamental throughout this journey and we learnt together how distance can make bonds either weak or strong, and

we freely chose the second option.

To all of my family, my mother, father, sister and brother: thank you for all the Taiga's pictures you sent me. You really can't understand how many times those pictures made me smile and helped me overcome discouragement moments. Of course, you are my foundation and my first home, a group of crazy individuals, my greatest supporters.

Manuel, there are no words to describe how your support has been of primary importance since I decided to pursue this dream. To you goes my sheer gratitude and love. We made it.

MAZ

TABLE OF CONTENTS

TABLE OF CONTENTS (continued)

CHAPTER **PAGE**

LIST OF TABLES

LIST OF FIGURES

LIST OF FIGURES (continued)

LIST OF FIGURES (continued)

LIST OF ABBREVIATIONS

ADC	Apparent DIffusion Coefficient
CPMG	Carr-Purcell-Meiboom-Gill
DTI	Diffusion Tensor Imaging
DWI	Diffusion-Weighted Imaging
FID	Free Induction Decay
FOV	Field Of View
ICNRIP	International Commission on Non-Ionizing Radiation Protection
MD	Mean Diffusivity
MEG	Motion Encoding Gradient
MR	Magnetic Resonance
MRE	Magnetic Resonance Elastography
MRI	Magnetic Resonance Imaging
NMR	Nuclear Magnetic Resonance
ROI	Region Of Interest
SAR	Specific Absorption Rate
SNR	Signal-to-Noise Ratio

LIST OF ABBREVIATIONS (continued)

TE	Echo Time
TR	Repetition Time
w/v	weight over volume

SUMMARY

Magnetic Resonance at low-intensity field has been employed mainly for NMR spectroscopy even though low-intensity field MRI scanners can be of small size and their use would allow lower artifacts impact, lower price and operational costs as well as lower SAR within very sensible samples. The present dissertation reports an analysis of both animal tissues samples and water-based solution carried out with a benchtop 0.5 T scanner. Relaxometry parameters were computed for liver and muscle samples and were found to be consistent with literature values and in agreement with an exponential model. Relaxation rates of liver (muscle) for T_1 and T_2 were 219 $\pm$ 3 ms (610 $\pm$ 8 ms) and 41 $\pm$ 1 ms (51 $\pm$ 1 ms), respectively.

A custom-made diffusion sequence was developed and measurements of ADC were carried out, and results suggest that a 20% gelatine could be useful as a liver and muscle phantom. Nevertheless, the sequence needs to be further improved in order to compensate for possible artifacts contributions. Muscle Mean Diffusivity values along the three orthogonal directions respected the known anisotropic water motion behavior.

Along with an MRI approach, a physical support for the piezoelectric actuator and an algorithm for the computation of the complex displacement maps from the MRE signal were created. The complex modulus for gelatine, liver and muscle samples was assessed: gelatine samples showed an increase of the average storage shear modulus with both frequency and also with higher concentration. Liver storage modulus ranged from 6.49 $\pm$ 1.53 to 19.67 $\pm$ 3.56 kPa in MEG

frequency range between 500 and 2000 Hz, while muscle storage modulus was one order of magnitude higher with respect to both liver and gelatine samples.

CHAPTER 1

INTRODUCTION

1.1 Magnetic Resonance

Magnetic Resonance Imaging (MRI) is a non-ionizing, non-invasive powerful medical imaging technique which provides tomographic images generated by the detection and processing of the Nuclear Magnetic Resonance (NMR) signal coming from the interaction of nuclei and an external magnetic field. This technique involves several advantages, including a good soft tissue contrast, high spatial resolution as well as patient acceptance and low risk [1].

The underlying physical principles of NMR is *nuclear magnetism*, a phenomenon that is achieved by placing a sample into an external magnetic field. While Felix Bloch and Edward Purcell (Physics Nobel prizes in 1952) first discovered and formalized nuclear magnetism, the rationale of image formation based on spatial encoding was established by Paul Lauterbur in 1972.

MRI is able to visualize high resolution anatomical images of soft tissues, resulting to be an optimal imaging technique that is nowadays exploited for the examination of brain, spinal cord, joints and liver for example, producing images of tumors and other pathological conditions in several districts of the body.

Although an exhaustive description of NMR phenomena should require a quantum physics based analysis, a semi-classical approach based on Newton's classical mechanics laws is also valid and more straightforward.

A nucleus is a spinning charged entity and, as such, according to Faraday's law of induction, cause the generation of a magnetic field around it. Given that hydrogen (protium ^{1}H) represents roughly 10% of human tissues and that the other principal elements constituting it are non NMR-active, the following dissertation will regard hydrogen. If not differently specified, a nucleus will refer to a single proton ^{1}H. Specifically, water protons will be considered. As for terminology, in MRI a *spin system* or *isochromat* is composed by a group of nuclei sharing the same precessing (Larmor) frequency and the same characteristics in terms of signal production. When a spin system is not immersed in an external magnetic field, thermal random motion results in a null net magnetic field around an object, which means that the macroscopic bulk magnetization $\vec{M}$, resulting from the sum of the microscopic magnetic moment vectors, has zero magnitude.

1.2 RF excitation

The bulk magnetization vector points along the static magnetic field B_0 direction and due to the stochastic phases of the precessing magnetic moments, the transverse component of $\vec{M}$ has zero magnitude. In order to reach the *resonance condition*, which is phase coherence among spin phases, an external energy coming from an oscillating magnetic field B_1 in the RF range (so called *RF-pulses*) should be applied and its energy has to correspond to the energy difference between adjacent spin states. For Planck's law the required radiation energy E_{rf} is

$$E_{rf} = \hbar\omega_{rf} = \hbar\gamma B_0 \tag{1.1}$$

(where $\hbar$ is the reduced Planck constant $h/2\pi$) since $\omega_0 = \gamma B_0$, called *Larmor frequency*, and in terms of angular frequency the resonance condition can also be defined as

$$\omega_{rf} = \omega_0 \quad , \tag{1.2}$$

in which γ is the gyromagnetic ratio, a physical constant possessed by spinning subatomic particles (for ^{1}H, $\gamma = 2\pi \cdot 42.58$ MHz/T).

In MR both system excitation and receiving is performed by using electromagnetic radiation in the RF range, non-ionizing radiation whose frequency is between 10^6 and 10^8 Hz.

The amplitude of the oscillating field B_1 is generally 2-4 times lower in order of magnitude with respect to B_0 and, since it oscillates along a single (x) axis, it is said to be linearly polarized. B_1 usually takes the form

$$\vec{B_1}(t) = 2B_1^e(t)\cos(\omega_{rf}t + \phi_0)\vec{i} \quad , \tag{1.3}$$

with $B_1^e(t)$ as the pulse envelope function and ϕ_0 as the initial phase. B_1 can be decomposed into two fields rotating on the xy-plane (perpendicular to B_0) with opposite directions, so to null the y component: while one of these fields rotates clockwise, the other one rotates counterclockwise which is also opposed to the direction of the precessing spins. This results in the Bloch-Siegert shift, a minor shift of the observed resonance, which becomes negligible for $\omega_{rf} \to \omega_0$ [2].

B_1 can then be written using the complex notation as follows:

$$\vec{B_1}(t) = B_1^e(t)e^{-i(\omega_{rf}t+\phi)} \tag{1.4}$$

considering the y-component as imaginary. Based on the duration and shape of an RF-pulse and gradient field, the exerted excitation differs in properties such as the resonating frequency bandwidth, slice thickness and the transverse magnetization. In order to excite a narrow frequency band and reach a high frequency selectivity, based on the Fourier transform asymptotic property, smooth pulses (so called "soft pulses") such as the Gaussian or sine pulses can be used. For a broad sample excitation, rectangular pulse ("hard pulses") may be used instead.
Since the effect of the application of the B_1 field is a rotating movement of the bulk magnetization $\vec{M}$ in the xy-plane, in MRI technology it is customary to use a non-inertial coordinate system (identified by the axes x', y' and z') called *rotating frame*, which rotates clockwise with angular frequency ω relative to the laboratory frame.
When $\omega = \omega_0$ the rotating frame rotates at the Larmor frequency and is then called *Larmor-rotating frame*, while when $\omega = \omega_{rf}$ it is called *RF rotating frame*; when resonance condition is reached, these two frames coincides and the bulk magnetization has a precessing motion with respect to the x'-axis with angular frequency $\omega_1 = -\gamma\vec{B_1}$. As a result of the excitation provided, at the end of the RF-pulse application the magnetization vector will be tilted of a (*tilt*) *flip angle* equal to

$$\alpha = \int_0^{\tau_p} \omega_1(t)dt = \int_0^{\tau_p} \gamma B_1^e(t)dt \quad . \tag{1.5}$$

1.2.1 RF pulses

When a RF-pulse is employed to reverse the direction of the magnetization vector from the direction of the main magnetic field to the other, that RF pulse is called an *inversion pulse* or

180° pulse. When the pulse flips the magnetization into the transverse plane, then it is called a 90° pulse. Based on the kind of RF-pulse (and in particular its shape) applied on the object under analysis, different kinds of signals will be acquired, bearing information from different spectral frequencies. In some sequences (as spin- or gradient-echo ones), some RF (dummy or preparatory) pulses are provided to the sample shortly before the main RF-pulses in order to have an equilibrium $\vec{M}$ value.

Different kinds of RF-pulse shapes are commonly employed in MR studies and the most common ones are either hard or soft pulses [2].

- *Hard pulses* possess a rectangular shaped waveform, and so a constant amplitude throughout their duration. No spatial or spectral selection is accomplished by the application of such pulses due to its broad frequency bandwidth, resulting in the excitation of a wide range of resonant frequencies.
- *Soft pulses*, on the other hand, are time-varying or time-shaped pulses. Sinc pulses (based on the cardinal sine function) are a particular kind of soft pulses which have been widely used in MR, and whose central lobe is wide as the double of each other lobe. Since the Fourier Transform of an infinite sinc function is a rectangular window, a uniform slice profile is then selected when such pulses are employed. In reality a truncation to finite length pulse is performed (apodization can be applied to ease the resulting effects) and generally, the higher the number of sinc lobes, the closer the frequency profile is to a rectangular window.

Then, on the base of the Fourier Transform properties, typically the selectivity property of a pulse is given by both its shape and its width. Pulses with constant RF amplitude are typically non-selective while pulses showing a modulation of their shape are usually frequency selective.

1.2.2 Sequence components and parameters

Besides the RF shape and duration, also other commonly used parameters characterize the kind of used sequence thus determining signal and image characteristics. Among these parameters, echo time and repetition time are two of the most frequently present ones: while *echo time* (TE) corresponds to the time from two consecutive RF-pulse centers, the *repetition time* (TR) is basically the length of a pulse sequence, so corresponding to the time window between sequence corresponding consecutive points [3]. Resolution, voxel dimension, acquisition time, sampling frequency, field of view (FOV) and slice thickness are also ubiquitary in MR image analysis, as part of the image processing glossary in general.

The introduction and spreading of diffusion MR also resulted in the need to unify a nomenclature and symbolism for diffusion parameters, such as the duration of the diffusion gradient, denoted as δ, and the interval from the beginning of the two successive diffusion gradient Δ. B-value (defined in Section 3.1) is also a fundamental parameter that needs to be taken into account.

The RF echo phenomena was discovered by Hahn in 1950: he found out that when multiple 180° pulses are applied, an echo signal can be generated (RF echoes). This can be achieved also by applying magnetic field gradient reversal, so to give gradient echoes.

When a 90° RF pulse is followed by a delay and another 180° RF-pulse, then the echo signal generated is called a *spin echo* and this is given by a restoration of the coherence between spin

magnetic moments given by the second pulse. Different combinations of angles and multiple RF-pulses may be applied, and time-varying gradient magnetic fields, which are able to cause signal dephasing and rephasing in a controlled way, are usually employed to generate another frequently used echo signal. In such case, small flip angle excitation are customary employed for a fast imaging and a negative x-gradient is applied subsequently the RF-pulse application [4]. Usually *pulse sequence* diagrams are employed in practice to represent amplitudes, timing and kind of RF-pulses and gradients provided to a sample. In fact, besides RF-pulses, gradients of magnetic field are of primary importance in magnetic resonance imaging since their aim is to spatially encode information in the nuclear magnetic signals that will be recovered during reconstruction. Such gradients are also used to calibrate image contrast to various types of motion (coherent or incoherent), to deal with image artifacts and to selectively choose NMR signals. [5].

1.3 Introduction to diffusion MRI

Magnetic field gradients can be used to confer specified contrasts to MRI signals: diffusion imaging exploits diffusion-weighting gradients to sensitize the MRI signal to molecular diffusion [6]. These gradients typically consists of two equivalent lobes and, when inserted in a spin-echo pulse sequence sequence at either side of a refocusing 180° RF-pulse, the two lobes share the same polarity, while in gradient-echo-based sequences they have inverse polarity.

When a diffusion-weighting gradient is inserted in a pulse sequence, water diffusion can cause proton MRI signal attenuation: the attenuation extent depends on the product of the diffusion

coefficient D and the b-value, a quantity that results from the gradient waveform and the whole pulse sequence diagram.

1.4 Magnetic Resonance Elastography

Palpation is a widely employed technique to detect abnormal stiffness changes in soft tissues, usually associated to tumors and fibrosis. Although popular, palpation is restricted to body surface, qualitative and subjective, thus prone to inter- and intra-subject variability. To overcome inaccessibility of deep tissues, ultrasound has been used for elasticity measurements, particularly for in vivo liver and skeletal muscles assessment, but biopsy remains the gold standard in detecting abnormal tissue and mechanical changes, even though invasive, sample-related and painful [7]. In recent years, Magnetic Resonance Elastography (MRE), an emerging high-sensitive and non-invasive medical imaging modality exploiting Magnetic Resonance phenomena, has been introduced to characterize tissues through their viscoelastic properties. MRE has been associated with a high sensitivity to viscoelastic constants - specifically the shear (complex) modulus - in pathological tissue alterations also at the onset of the variation. Such parameters arise from hierarchical organization in biological tissue and so MRE is exploited for analysis in degenerative neurological disorders, heart diseases, tumors and all fibrotic diseases, included hepatic fibrosis [8]. Among stiffer tissues, which are more resistant to mechanical deformation, it is possible to find contracted muscles, fibrotic liver, cerebral tissues of young subjects and healthy brain (with respect to brain affected by multiple sclerosis, normal pressure hydrocephalus and Alzheimers disease) [9]. MRE provides similar shear modulus values to those of oscillatory rheometry, which is a well known method for the study viscoelastic materials [10]. In MRE, a

phase contrast MRI method is used to measure shear waves - waves whose direction of displacement is perpendicular to the direction of propagation - resulting from such harmonic or periodic mechanical excitation propagating in tissue. This allows a direct visualization at low audible frequencies (<5kHz) to consequently assess local values of shear modulus of tissues. Once displacements are measured, both speed and attenuation of shear waves can be computed, while for a simple isotropic (elastic) Hookean material, stiffness, expressed by its shear modulus, is a function of shear wave speed c. So once c has been computed, then the shear modulus is

$$\mu = \rho c^2 \tag{1.6}$$

with density ρ. Shear modulus is an absolute quantity that does not vary with the excitation frequency under the elastic assumption, but does so under the assumption of viscoelasticity. Shear wave speed is normally expressed as

$$c = \lambda f \tag{1.7}$$

with λ wavelength and f frequency. λ may be used to the tissue stiffness computation, and Equation 1.6 suggests that a stiffer material will propagate waves faster, and thus will show a longer wavelength. The sensitivity of wavelength to elasticity changes can be employed to discern elasticity variations, since local wavelength changes correlate to local changes in terms of mechanical properties. A more complex analysis is needed when the elasticity and isotropy

assumption are no longer valid.

1.4.1 Soft tissue properties

For soft tissues analyzed in the frequency spectrum that is usually employed in MRE analysis, compression waves speed is around $1540 m/s$, which undergoes small variations in different tissue types. Shear waves instead propagate with much slower speed (this is linked to the shear modulus properties) and is typically around $1-10 m/s$ and that, on the other hand, is seen to vary consistently between tissues. This makes shear properties preferable targets for elastographic investigations as compared to compressional properties [9]. Soft tissues exhibit both elastic and viscous mechanical behaviors [11]. For such materials, stress-strain relationship varies over excitation time. Viscoelastic materials show three peculiar mechanical characteristics:

- Viscoelastic creep - increasing of strain with time during the application of a stress (externally applied load);
- Viscoelastic relaxation - decreasing of stress when a constant strain is held;
- Dissipation of mechanical energy as heat during cyclic loading;
- Frequency-dependent complex shear modulus.

Elastographic imaging methods have been proposed as a valuable method to represent the mechanical properties of viscoelastic materials, which may also involve parameter fit ting (attenuation coefficients and shear-wave speed) to rheological models. [12]

1.4.2 Transversely isotropic models

While homogeneous materials such as gelatines present a mechanical isotropic behavior, transversely isotropic materials present a preferential direction in which material response to excitations is different from that on the orthogonal directions, so to define an *isotropy plane*. Skeletal muscles, for example, exhibit a response to a stress along the direction of the muscle fibers which is different to the one that a stress provided transversely would result into.

A transversely isotropic model establishes the simplest anisotropic model. While five parameters are needed to define such material type, only three are enough to completely define an incompressible material that is also transversely isotropic [13] [14].

Transversely isotropic models are appropriate in characterizing mechanical properties in biological tissues such as the skeletal muscles [15]. Several studies in scientific literature assumed that very soft tissues, such as liver tissue, are essentially mechanically isotropic [16]. This is supported by Diffusion-Weighted Imaging studies of liver that show that water molecule motion has been found to be isotropic in healthy liver [17] while diffusion for muscle fibers results to be anisotropic and preferentially oriented along fiber direction [18].

1.5 Structure and physiology of liver and skeletal muscle tissue

1.5.1 Skeletal muscle

Skeletal muscle is a transversely isotropic soft tissue whose mechanical properties generates are rooted in the alignment of parallel fibers which are found packed in muscular fascicles. Myofibrils arrangement, enclosed by the sarcolemma, provides skeletal muscle with its striated pattern which is discernible even macroscopically at naked eye.

Since muscle bundles are found to be grouped in geometrical fashion which is replicated at hierarchical levels, skeletal muscle may be mathematically referred to as a fractal structure.
As a soft tissue, muscle can be considered a viscoelastic material and its density is very close to water density ($\simeq$1g/cm^3) as many tissues present a bulk modulus within a 15% range centered on water value [19]. Muscle also shows a non-Hookean behavior if excited with large deformations and the value of Poisson coefficient is close to 0.5 (incompressibility situation) since bulk modulus E is estimated to be approximated 3 times muscle shear elasticity μ ($E = 3\mu$).

1.5.2 Liver

The liver is the largest body gland, with both endocrine and exocrine functions. In humans, the liver anatomically consists of four lobes: the right and left ones (the larger ones), the quadrate and the caudate (the smaller ones) [20]. These lobes are surrounded by a capsule constituted by connective tissue, while every lobe consists of lobules which are separated one from the other by a thinner connective (Glisson's) capsule.
Liver structural plan is determined by its vascular supply since, within the lobules, blood travels between hepatic cells in sinusoids toward a central vein. [21]. Liver functional unit is the hepatic acinus, with its center corresponding to the two portal triads and the outer bounds defined by two adjacent central veins. Although a repetitive functional structure, such as the hepatic lobules which is present and delineated by connective tissue, isotropic models have been studied for liver MRE applications including either viscoelastic or elastic properties [13], considering then liver as a mechanically isotropic tissue. This is also supported by DWI because water diffusion in the liver parenchyma, which is found to be isotropic [22].

1.6 Low magnetic field intensity

Research at low magnetic field intensity has been employed in particular for NMR spectroscopy while few applications to the clinical field can be found in scientific literature. Although 1.5T (and higher intensity) superconducting magnets dominate the MR marketplace, and an increase in magnetic field strength leads to an improvement in SNR ratio and to an increased resonant frequency dispersion [23], lower field (research) scanners come with advantages [24] such as:

- *Lower initial purchase price and operational costs*: as scanner price increases with field intensity, also power supply costs, special maintenance and Helium cryogenics are usually needed for high permanent field intensity magnets;
- *Lower fringe field*: lower field scanners are easier to site and shield (from projectile risks) within a research environment. As electromagnetic force is proportional to the magnetic poles magnitude and decreases with the square of the distance, equipment and instrumentation may be brought closer to a low-field scanner.
- *Reduction of MR artifacts* such as chemical shift and motion (and flow) artifacts are often less apparent on images from lower field scanners
- *Lower energy deposition in tissues*: the energy given by RF-pulses and deposited in tissues (also called SAR, from Specific Absorption Rate) is proportional to the square of B_0 and is linked to possible dangerous heating.

It may then be interesting to investigate the applicability of such low magnetic field intensity scanners for to the pre-clinical reality and carry out analysis of tissue samples in both MRI and MRE spheres.

1.7 Motivation

Magnetic Resonance Imaging stands out compared to other imaging technologies, as the MRI signal can be tuned sensitive to a variety of contrast parameters. The present dissertation is aimed at showing the potentialities of the exploitation of a benchtop 0.5T Magnetic Resonance device for the characterization in terms of relaxation parameters, of diffusion parameters and also through an elastography based analysis.

Since SNR is proportional to nuclear spin polarization, linearly scaling with the static magnetic field strength, high-field intensity magnets would be unequivocally preferred and yet several financial and technical issues would rise, disadvantages that a low-field MRI may mitigate and overcome.

The discussed MR scanner comes with low operational costs, little space demands and a high practicality and usability - given by the possibility to easily customize and develop pulse sequences, as well as process the acquired data. Provided what has just been stated, there is increasing interest in understanding the potentials of such devices as well as investigate their limits. Future applications of a benchtop device could also be its employment in intra-operative surgery or generally as an exploratory tool in the magnetic resonance domain for small samples. While for relaxometry and diffusion imaging low-intensity magnetic fields have been studied so far, especially for spectroscopic analysis, in scientific literature MRE experiments of tissue

samples of small dimensions have been conducted mainly with high-field scanners, although some trials at low-field [53] have been performed. Here a tissue sample investigation is carried out with a newly developed benchtop MR scanner setup.

CHAPTER 2

NMR RELAXOMETRY

2.1 Bloch equation

Dynamics of the magnetization vector is described by the Bloch equation [26], named after the Swiss physicist who discovered it (awarded the Nobel Prize for Physics with Purcell in 1952).

The expression in vectorial terms of this equation in the laboratory frame is

$$\frac{d\vec{M}}{dt} = \gamma\vec{M} \times \vec{B} - \frac{M_x\vec{i} + M_y\vec{j}}{T_2} - \frac{(M_z + M_z^0)\vec{k}}{T_1} \quad , \tag{2.1}$$

where M_z^0 is the intensity of the bulk magnetization $\vec{M}$ at thermal equilibrium, T_1 and T_2 are the relaxation times, further described.

With respect to the rotating frame, the relaxation processes can be seen as first-order processes whose time constants rule the equations:

$$\begin{cases} M_{z'}(t) = M_z^0(1 - e^{-t/T_1}) + M_{z'}(0_+)e^{-t/T_1} \\ M_{x'y'}(t) = M_{x'y'}(0_+)e^{-t/T_2} \end{cases} , \tag{2.2}$$

in which 0_+ refers to RF-pulses application end time (and the terms with 0_+ are linked to the cosine of the tilt angle). In the laboratory frame the transverse magnetization has an exponential decay ruled by a e^{-t/T_2} and a precession term $e^{-i\omega_0 t}$. As further discussed herein the

length of the free precession period is dependent on the T_2 value and, as a matter of fact, it can be always stated that $T_1 \geq T_2$ [30].

Relaxation can be intended as the process by which the excited nuclei release the energy provided by RF-pulses. T_1 and T_2 are the time constants (called *relaxation times*) ruling the increase of the longitudinal magnetization and the decay of the transverse magnetization signal (FID), respectively and both of them are defined as the time needed to approach by the 63% (corresponding to $1 - e^{-1}$) the final value after a 90°-pulse. The inverse value of a relaxation times is the *relaxation rate* R and when considering a solution with varying concentration of contrast agent, the term *relaxivity* r stands for an R value normalized by the contrast agent concentration (reduced relaxation rate). Both relaxation times and the derived measurements are influenced by factors such as temperature (according to Boltzmann relationship) and contrast medium concentration [27]. T_1 is also dependent on the magnetic field intensity while proton T_2 relaxation in bulk materials (such as tissues and gels) is basically influenced by magnetic field inhomogeneities and not being significantly determined by fast motion processes. So T_2 in such systems can be considered as almost frequency independent [28].

The T_1 and T_2 relaxation times describe physical processes that influence the behavior of spin magnetic moments. In bulk materials (such as water, gels, tissues) these processes are influenced by molecular motion, rotation and translation. As the individual spins move with respect to each other their respective magnetic fields interact such that spins themselves influence the return to equilibrium state.

T_1 is commonly known as the *spin-lattice* or longitudinal relaxation time: it measures molecular

motion of the lattice in the proximity of the excited protons. The closer ω_0 is to the lattice angular frequency $\omega_{lattice}$, the faster and more efficient is the energy transfer and lower T_1 will be [29]. For most protein constituting the tissues $\omega_{lattice} \simeq 1$ MHz so, considering the most common static field intensities in clinical scanners (around 1.5 T - 3 T), T_1 decreases with B_0 intensities as the energy transfer gets more efficient.

T_2 is commonly known as the *spin-spin* or transversal relaxation time and this term refers to energy transfer among nearby protons sharing the same molecular environment and with precession frequencies close or equal to ω_0. The actual transverse relaxation time that can be computed is given by several contributions: after a 90° RF-pulse has been applied, coherence of the spins is found on the xy-plane and the system loses its coherence as time elapses.

A loss of coherence in the xy-plane is given by inter-molecular and intra-molecular motion, either vibratory and rotational, which causes the magnetic field not to be fully homogeneous or uniform, resulting in changes in ω_0 for protons. B_0 nonuniformities come from both constant and transient sources: imperfections in magnet manufacturing, interactions with metals (such as the magnet case) and sample-induced inhomogeneities due to differences in the magnetic susceptibility or the presence of imaging gradients (an induced and transient field inhomogeneity). The total reduced transverse relaxation rate T_2^* is then given by

$$T_2^* = \Big(\frac{1}{T_2} + \frac{1}{T_{2,i}} + \frac{1}{T_{2,s}}\Big)^{-1} \quad , \tag{2.3}$$

where $T_{2,i}$ is related to inhomogeneity in the magnetic field while $T_{2,s}$ is related to differences in magnetic susceptibility.

As the repetition time (TR) increases, the thermal effect has a higher impact on the measures since dephasing and loss of coherence would contribute to a decrease in signal intensity. Longer TRs lead to an increase in SNR and generally TR is chosen to be longer than three-five times T_1 [30] for accomplishing the (almost) full recovery of the bulk magnetization at equilibrium.

Commonly T_2 values are computed as the slope of the regression line of the natural logarithm of the signal intensity following a pulse sequence. Sometimes a multi-exponential function (given by the sum of two exponentials) could be used for a better fitting especially when analyzing samples in which there are different proton densities and T_2 times but when choosing TR greater than TE [30].

The Nuclear Magnetic Resonance Dispersion (NMRD) profiles report the field dependence of T_1 on B_0, representing water proton variability in relaxation properties as a static magnetic field strength function. NMRD profiles can be obtained by the application of an extended range of Larmor Frequencies with a dedicated Field Cycling NMR relaxometer.

MRI phantoms are essential for calibration and checking of MRI equipment as well as for the development of pulse sequences, new systems and training of MRI operators. Two kinds of MRI phantoms are generally used, aqueous solution or jelly-like materials. While jelly-like phantoms include gelatine, agarose, agar, PVA and other materials which are used for instrument validation, aqueous solutions of paramagnetic ions containing $CuSO_4, NiCl_2, MnCl_2$ or $GdCl_3$ are normally used for checking MRI equipment because of their homogeneous relaxation times and

long-term stability [31].

2.2 Relaxometry - Gadolinium based contrast agents

The inherent soft-tissue contrast allows to distinguish different tissues in MRI without any exogenous contrast agents for a wide range of diagnostic purposes. When this contrast is not sufficient to fully characterize the investigated tissues unambiguously, then MRI contrast agents may be used. These substances have the aim to improve the visibility of internal body structures with respect to their surrounding in MRI analysis. An ideal phantom for relaxometry measurements would require features such as independence of the relaxation times upon temperature and B_0 intensity, long-term stability and ease of preparation. In practice, minimal dependence of the relaxation parameters on temperature and frequency is considered and greatly convenient [28].

Contrast agents may be subdivided into two categories:

- *Paramagnetic compounds*, which present lanthanides (as Gd) that reduce the longitudinal relaxation time. They are sometimes called "positive contrast agents";
- *Superparamagnetic magnetic nanoparticles* with a strong effect on T_2. They are usually called "negative contrast agents"and are satisfactorily employed for MRI analysis and sequences weighted on the (reduced) transversal relaxation time. [1] [27].

Water solutions of gadolinium paramagnetic complexes are widely used nowadays as contrast agents to boost MRI diagnostic capabilities [29] since when paramagnetic solutes are found in

a water solution, the water proton relaxation rates result from the sum of the contributions of both the diamagnetic relaxation rate and the paramagnetic one (water). Furthermore, when no interactions between solutes take place, relaxation rates are found to be linearly dependent on the contrast agent concentration [32].

For the most commonly used MR contrast agents, the highest reduction of the transverse relaxation rate is found in a range between 295−315 K [29] [33]. Gd−BOPTA (gadobenate dimeglumine, MultiHance®, Bracco, Italia, Figure 1) is a paramagnetic descendant of Gd−DTPA (Magnevist®, Schering AG, Berlin, Deutschland), being a second-generation contrast agent. MultiHance concentrations higher than 1 mM has been observed to result in a nonlinear relationship between relaxation rate and concentration up to 3T [34].

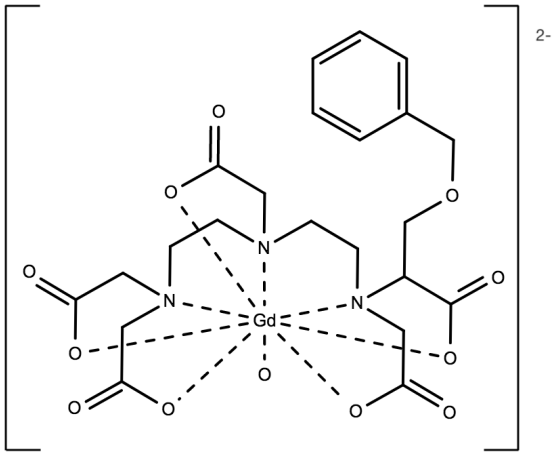

Figure 1: MultiHance molecular structure.

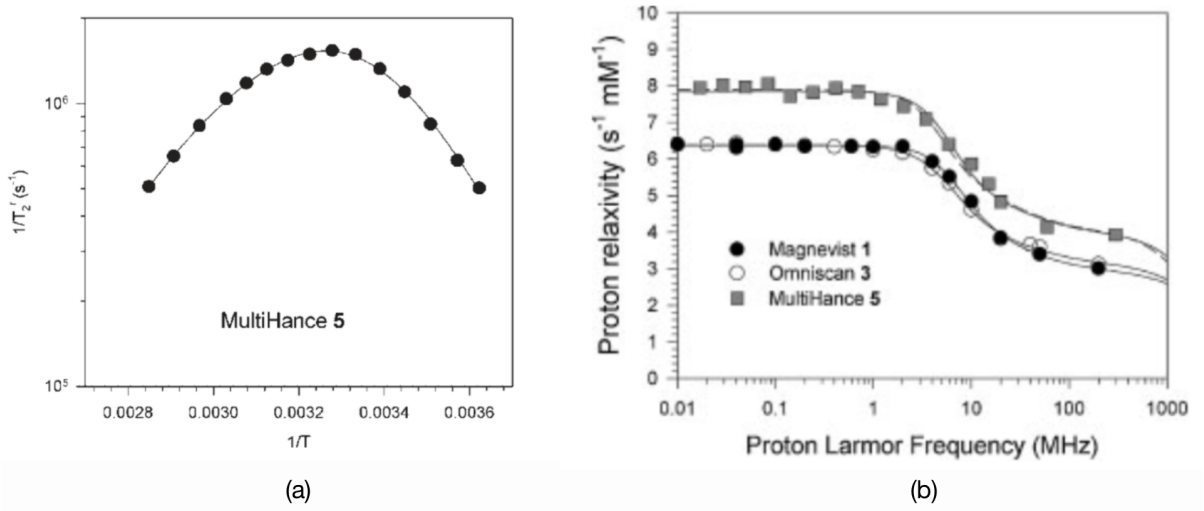

Figure 2: (a): MultiHance transverse relaxation rate for varying temperature at 7.05 T. (b): MultiHance NMRD profile, showing transverse relaxivity measured in water solution at $310K$ for different values of B_0 intensities, which is equivalent to the Larmor frequencies. Credits to the authors [Laurent et al.].

To our knowledge, relaxivity values for water solution of Gd-BOPTA have always been measured in a range of temperatures which are clinically relevant, not at room temperatures at standard laboratory conditions: since contrast media find their use in living subjects, the most commonly employed testing temperature is 310 K, corresponding to human body temperature. The most investigated solutions of Gd-BOPTA are of Human Blood Plasma [35] which usually show higher values for both the longitudinal and the transverse relaxivity with respect to water solutions of the substance [27] [34]. Considering a temperature of 310 K, a static magnetic field intensity around 0.47 T and concentrations not exceeding 1 mM, values for T_1 relaxivity are found around 4.2 $\mathrm{Lmmol^{-1}s^{-1}}$, while values for T_2 relaxivity at the same condition are around

4.8 $\mathrm{Lmmol^{-1}s^{-1}}$ [27]. Further studies have employed Human Blood Plasma samples, for which $r_1 \simeq 9.2 \pm 0.5 \mathrm{Lmmol^{-1}s^{-1}}$ and $r_2 \simeq 12.9 \pm 0.9 \mathrm{Lmmol^{-1}s^{-1}}$ are found [27].

Both longitudinal and transverse relaxation times are enhanced with respect to the other gadolinium agents which has been shown to translate into superior contrast efficiency and performance for MR applications in many body regions such as the central nervous system, breast, liver and vascular system [34].

2.3 Relaxometry - Animal tissues

In tissues, the dependence of water proton spin-lattice relaxation rate R_1 $(1/T_1)$ is due to the magnetic coupling of the tissue components with protons [36]. A variety of biomolecules (lipids, saccharides, nucleotides, proteins) may contribute to T_1, but proteins may be considered as the dominant factor determining relaxometric properties in most tissues and so purified protein systems may be employed as a proton spin relaxation model for tissue systems [37]. As a matter of fact, the increase of tissue water proton T_1 with increasing static magnetic field intensity is given by the simultaneous decrease of tissue spectral density at the applied Larmor frequency [23]. For a specific type of tissue, no significant difference in correlation between T_1 and B_0 intensity has been found in species in species. On the other hand, T_2 in biological tissues is considered to be essentially independent of B_0 field intensity while mainly dependent on tissue type; typical values are found to be on the order of tens of milliseconds [38].

As for [37], for solid samples such as tissues the spin-lattice relaxation rate R_1 is described by a power law

$$\frac{1}{T_1(\omega)} = A\omega^{-b} + C \tag{2.4}$$

where A is a constant related to the relaxation-driving dipolar couplings, while b is usually in the $0.5 - 0.8$ range and C represents the plateau value at high field intensities. This equation shows a relatively weak monotonic decrease of R_1 with growing magnetic field intensity For some animal tissues also two other terms have been added to the model [36]: a logarithmic term associated with water diffusion in interface regions (at high macro-molecular concentration this effects is significant) and a constant term related to water spin-lattice relaxation limit at high frequencies.

For muscle tissue, the value of b is found between 0.51 and 0.65 while C ranges from 0.3 to 0.4 s^{-1} and similar values have been estimated in kidney and liver. The computation of C has been sometimes avoided by considering a R_1 constant derivative and this has produced b values of 0.6 ± 0.1 [36].

CHAPTER 3

DIFFUSION MRI

During the 1950 experiment performed by Hahn, new evidences of the existence of different factors influencing the magnetization signal given by proton motion were found. The major discovery was that after a 180° RF-pulse, the generation of an echo signal – given by the rephasing of the spins – depends on those spin-bearing molecules which remain in the same local field over the whole process. Among the dephasing factors, *diffusion* is acknowledged and it is defined as the process by which random molecular motion - also called *Brownian motion* - is able to transport matter in a system. In a free medium, isotropic diffusion is customary to happen: in such a case, molecules can diffuse freely in all directions since no preferred direction for diffusion exists [18].

Statistically, diffusion can be estimated by the mean-squared distance $< X >$ traveled by molecules in a given time interval as expressed by Einstein's equation

$$< X >^2 = 2DT_d \quad , \tag{3.1}$$

in which D is the diffusion coefficient and T_d is the diffusion time. Diffusion NMR is then noninvasive and can be used to probe molecular dynamics, transport processes and structural information of biological systems, where spins may be considered as endogenous tracers that can be traced in a similar way in a medium. While the original Hahn experiment employed two 90°

RF-pulses, later in 1954 Carr and Purcell showed the advantages to use a train of 90° followed by a train of 180° RF-pulses, but Meiboom and Gill (1958) suggested the application 180° RF-pulses with phases shifted in quadrature with respect to the first 90° pulse to maintain the reversibility of the phases throughout the echo train - which is spoiled by RF field imperfections. Sequence is this known as the CPMG train, from the initials of its developers. In order to quantitatively show diffusion and flow impact in terms of transport of magnetization, in 1956 Torrey then introduced two additional terms in Bloch equations, so that the spatial and time evolution of transverse magnetization equation, in the rotating field, could be expressed as

$$M_+(\vec{r},t) = E(t)\exp\Big(-i\vec{r}\gamma\cdot\int_0^t \vec{g}(k)dk\Big)\exp(-t/T_2) \quad , \tag{3.2}$$

where $\vec{r}$ is the position vector, $\vec{g}$ is the gradient of the pulsed gradient field component parallel to B_0 and $E(t)$ represents the echo amplitude at the echo center (normalizing for the effect of T_2 relaxation). $E(t)$, in particular, is composed of two main exponential terms, so that both diffusion and flow effects are easily detectable within its own expression; because of phase incoherence arising from stochastic Brownian motion, diffusion causes attenuation of the echo signal, while coherent motion associated with flow enhances phase shifts.

3.1 Diffusion sequence

Since diffusion can be acquired without specialized hardware, it can be performed in the same setting along with conventional MR sequences [18]. Stejstkal and Tanner demonstrated in 1965 that the application of rectangular gradient pulses (Pulsed Field Gradient method)

during the dephasing and rephasing parts of the echo sequence (but not during the RF-pulse transmission) could be useful for the enhancement of the echo signal [39], as suggested by McCall, Douglass and Anderson in 1963. A $90°_x$ and a $180°_y$ RF-pulses are typically used and the echo amplitude at the echo center is

$$E = \exp(-\gamma^2 g^2 \delta^2 [\Delta - \delta/3] D) \exp(i\gamma\delta\vec{v} \cdot \vec{g}\Delta) \quad , \tag{3.3}$$

with δ as the duration of the gradient, and Δ as the time span from the beginning of the two successive diffusion gradients. With the use of a Pulsed Field Gradient Spin Echo (PFGSE), by far the most widely used for diffusion MRI, echo attenuation is then given by the factor $\exp(-\gamma^2 g^2 \delta^2 [\Delta - \delta/3] D)$ where free diffusion only is taken into account. In this kind of sequence, which is basically a spin-echo sequence, the applied diffusion gradients are added (and in the case of pulse sequence they would be in quadrature one to another). They get to be essential for MR Diffusion Imaging: while the first gradient results in a proton phase shift, depending on their positions, the second gradient reverses the phase given by the first gradient. If diffusion is present, the second gradient will not be able to completely undo the changes induced by the first gradient since diffusion causes the refocusing to be incomplete, leading to signal attenuation.

Also, the intensity of the gradient pulses determines the minimum diffusion path detectable so that hardware capable of providing stable gradient of very high amplitude needs to be used. A problem that has to be taken into account in designing a diffusion sequence is that increasing Δ involves increasing TE and thus substantial signal loss occurs through T_2 relaxation. Diffusion

MR imaging has been developed since the 1980s and has focused mainly on the investigation of neurological disorders, acute brain ischemia and oncology, conditions leading to an alteration of diffusion patterns.

Figure 3 shows a diffusion sequence with its timing conditions.

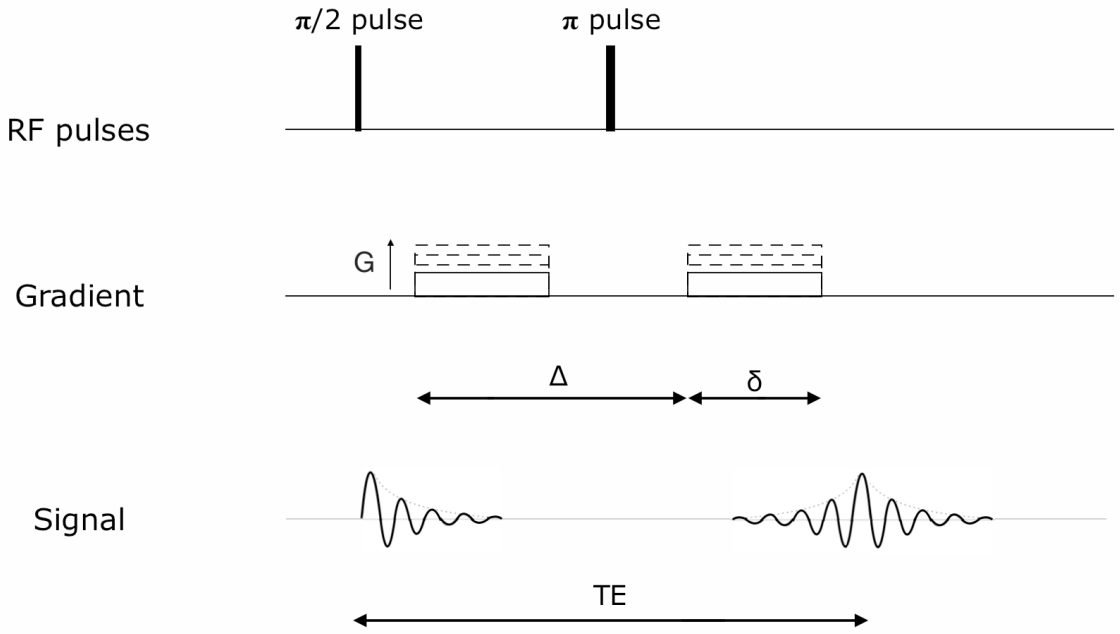

Figure 3: A typical diffusion sequence: diffusion gradients are applied symmetrically with respect to the π RF-pulse. In order to vary the b-value either the gradient amplitude G or gradient separation time Δ is varied.

For this reason the concept of b-value (or b-factor) has been introduced (from Le Bihan and Breton in 1985) for summarizing gradient effects. B-value is defined as

$$b = \gamma^2 \int_0^{TE} \Big[\int_0^t \vec{G}(t\prime) dt\prime \Big]^2 dt \tag{3.4}$$

and signal attenuation can be expressed by the exponential function of the echo signal

$$S = S_0 \exp -bD \quad . \tag{3.5}$$

With regard to imaging gradients, diffusion effects are negligible because such gradients have very low b-values per se, typically around 1 s/mm^2. Movement in the microvasculature can be seen as a pseudo-diffusion process at higher scale. While the spatial scale difference between pseudo-diffusion and actual diffusion extends over five orders of magnitude, the respective coefficients differ by just one order of magnitude [40]. It is clear that in-vivo diffusion measurements with MRI may include perfusion effects, which is expected to be present with very low b-values (< 200 s/mm^2). An overestimation of the true diffusion coefficient D could be achieved when the estimation of the diffusion coefficient itself is performed for only two b-values as conventionally done in clinical studies. In the context of diffusion MRI in in-vivo tissues, pseudo-diffusion processes given by complex intravoxel incoherent motion (IVIM) occurring with perfusion in

the microvasculature in biological tissue along with real diffusion have been jointed in a comprehensive parameter, the *Apparent Diffusion Coefficient* (ADC), that is

$$ADC = -log(S/S0)/b. \tag{3.6}$$

ADC is expressed in unit of mm^2/s, where S_0 and S are the echo signal intensities without any diffusion weighting gradient and the attenuated one with the employed b-value, respectively. Pseudo-diffusion arises from blood water flow in randomly oriented capillaries, inducing a signal attenuation during the application of diffusion encoding gradient pulses, particularly visible when applying very low b-values. When reporting ADC values, the respective b-values used for their measurements need to be reported [41].

Although larger b-values are linked to a higher water diffusion sensitivity, in terms of ADC, signal intensity decays exponentially with respect to b-value and high b-values results in an overall decreased SNR which may render the calculation of ADC inaccurate and unreliable.

The physical model used to establish the signal attenuation assumes a free, infinite and homogeneous medium but when diffusion is not free or when the medium is compartmentalized, deviation from theory can be expected. In particular deviations from free diffusion are particularly visible in anisotropic tissues whose histology show a uniform fiber pattern, such as white matter and muscles, in which free diffusion is impeded in the transversal direction of the fiber axis, resulting in an anisotropic water diffusion. For these tissues, diffusion is no longer free since it becomes hindered by obstacles and its directionality mainly depends on both tissue

cellularity and cell integrity [18]. Water molecules move in both the intra- and extra-cellular spaces, so macromolecules and cell membranes impede motion [42].

Diffusion coeffiecient then reflects interactions of water with tissue features and, furthermore, diffusion effects are strongly dependent on the direction of the gradient pulse. Diffusion MR imaging is exquisitely sensitive to tissue structure so that feature has been exploited to generate tractography maps, reporting the tridimensional orientation of white matter fibers for example [43].

3.2 Diffusion tensor

If compared with other parameters as T_1 or T_2, diffusion is merely a physical process occurring in tissues and not linked to MR phenomena. Diffusion parameters are tissue parameters, while relaxometry parameters are given by magnetic resonance phenomena and are depending on the field strength and MR imaging sequences [43]. Diffusion MR and so ADC values should be in principle independent on the employed MR imaging system, but when diffusion is non-Gaussian, such as in fibrous tissues, for increasing b-values the influence of diffusion-related signal attenuation decreases. Also different time profiles could lead to different diffusion effects while sharing the same b-value because water molecules will interact with tissue microscopic features when long diffusion times are used, giving lesser attenuation and smaller ADC values. Valuable information about clinical status, tissue microstructure and histological organization can be extracted by MRI measurement of water diffusivity in soft tissues. While isotropic diffusion occurs in pure liquids, for more complex media such as gels, colloids and biological tissues, a single self-diffusivity coefficient is no longer exhaustive for the description of diffusive

transport. Tanner introduced the notion of *ADC* as the diffusivity that can be computed by using the Stejskal and Tanner formula if the displacement distribution was Gaussian.

The measurement of an *ADC* is obtained from the projection of all molecular displacements onto the axis along which the diffusion gradients are applied. Diffusion is a process which occurs in the three-dimensional space and molecular mobility may be anisotropic, since substance physical arrangement can be different in all directions and then result in a different diffusion behavior when gradients are applied along varying directions. This has been observed in muscle [44]. To fully characterize diffusion, the symmetric *diffusion tensor* $\underline{\underline{D}}$ is introduced: it describes molecular mobility and correlations in 3D (Figure 4).

While the main diagonal elements represent diffusion coefficients measured along the normal laboratory axes, the other six off-diagonal terms reflect the correlation of random motions between each pair of principal directions. The off-diagonal elements all zero in case of a perfect isotropic diffusion (as for pure liquids). In such a case, the diagonal elements are all equal to a single diffusion coefficient D (i.e., $D_{xx} = D_{yy} = D_{zz} = D$). For anisotropic materials, instead, diagonal elements are different and the off-diagonal elements are non null. Furthermore, it has to be taken into account that the frame of reference affect the value of each tensor element and in order to estimate all of them, at least 7 measurements should be performed: one baseline (with b-value $b_0 = 0$ mm^2/s) and 6 other acquisitions (since there are 6 unknowns due to tensor symmetry).

The diffusion ellipsoid provides an ideal frame of reference for the computation of the diffusion

tensor: its main axis is parallel to the main diffusion direction and usually it is found along anatomic features such as muscular fascia, white matter tracts or general fascia planes.

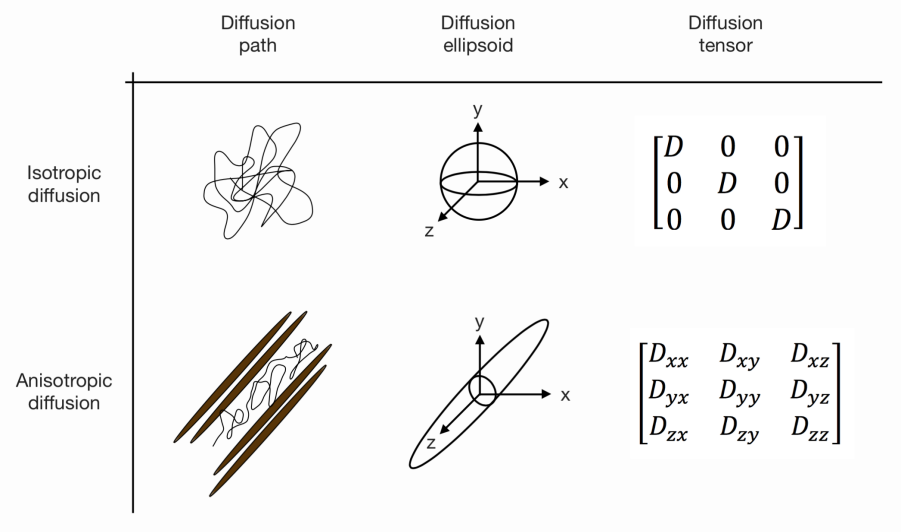

Figure 4: Diffusion tensor for isotropic and anisotropic scenario.

The average value of the tensor trace, $D = \dfrac{D_{xx} + D_{yy} + D_{zz}}{3}$ represents the orientation-averaged diffusion, sometimes called mean diffusion (MD). Trace is evaluated for example in liver Diffusion Weighted MR, by using tri-directional diffusion gradients along three non-collinear directions.

MD is rotationally invariant and results to be a measure of diffusion magnitude. Trace divided by three is equivalent to the tensor eigenvalues average, where the eigenvalues in the diffusion

tensor represent its 3 principal axes.[46]

MD typical values for healthy muscle are found to be around 1.3-1.4 $\cdot 10^{-3}$ mm^2/s [47] while for healthy liver they are found to be around 0.7-0.8 $\cdot 10^{-3}$ mm^2/s. The orientation of the fibers within a tissue can then be derived through DTI and visualized with Tractography; researchers have already employed DTI to track fibers (white matter) in human brain in order to generate white matter tract maps. So the use of DTI, resulting in information of fiber direction, can find application in MRE studies to allow estimation of the mechanical properties in both axial and transversal fiber direction, assuming a transversely isotropic model [7].

CHAPTER 4

MAGNETIC RESONANCE ELASTOGRAPHY

Quantitative elastography can be divided in three main steps:

- First, the application of induced motion or a stress to deform the tissue. Either internal or external stress sources can be considered, which may be harmonic or transient.
- Then tissue response to the stress is imaged, which is typically represented in terms of velocity or displacement either through ultrasounds, optical techniques or MRI, as in the case of *Magnetic Resonance Elastography* (MRE).
- Finally, an inversion algorithm has to be employed to process the data. Images of the mechanical properties of the tissues (also called *elastograms*) are so generated.

Harmonic MRE is the most common form of MRE imaging: it utilizes time-harmonic motion in the audible range (below 20 kHz) introduced through an external vibration source consisting of actuators such as electromechanical voice coils, piezoelectric materials or pneumatic-based actuators [9].

Phase-contrast images (either 1D, 2D or 3D) are acquired by applying classical MR sequences (through a gradient- or spin-echo imaging sequences for example) jointly with a *Motion-Encoding Gradient* (MEG) whose purpose is to efficiently encode the imparted motion. The mechanical vibration of actuator has to by synchronized with the MEG.

In order to obtain displacement images, phase data need to be scaled by the encoding efficiency, which is defined as

$$\xi = Y_0/\phi_0 \quad , \tag{4.1}$$

where Y_0 is the displacement amplitude and ϕ_0 is the amplitude of the MR signal. The phase signal is defined as

$$\phi(s) = \gamma \int_s^{s+\tau} \vec{K} \cdot \vec{u}(t, \vec{r}) dt \quad , \tag{4.2}$$

where $\vec{K}$ is the MEG, $\vec{u}$ is the displacement vector with amplitude Y_0, s and $s + \tau$ being the first and final temporal instant of the MEG application constituted by q MEG cycles, so that $\tau = 2\pi q/\omega$. In this way, the state of tissue displacement is encoded into the phase of MRI signal.

4.1 Wave equations

Wave propagation patterns are analyzed in an elastographic-based investigation, so what follows is an overview of the description of mechanical waves.

The Navier's wave equation of motion of an isotropic solid, under the assumption of infinitesimal deformations, small additional stresses and local homogeneity, can be written referring to a Cartesian coordinate system as

$$\rho \frac{\partial^2 \vec{u}}{\partial t^2} = (\lambda + 2\mu)\nabla\nabla \cdot \vec{u} - \mu\nabla \times \nabla \times \vec{u} \quad , \tag{4.3}$$

where ∇ stands for the gradient operator while $\vec{u}, \lambda$ and μ are the displacement vector, the first Lamé parameter and the second Lamé parameter (*shear modulus*), respectively.

In the isotropic scenario described in Equation 4.3, only two (Lamé) parameters are needed to fully characterize the object (tissue) under analysis, while in the most general anisotropic scenario 21 parameters are necessary to describe the mechanical behavior and these 21 independent elastic constants are found in the Christoffel rank-four tensor C present in the stress-strain $(\sigma - \epsilon)$ tensor relationship $\sigma_{ij} = C_{ijkl}\epsilon_{kl}$ [11]. For transverse isotropy in linear elastic materials stress-strain relations can be reduced to 5 material constants because of symmetry: the transverse isotropic material represents the lowest degree of anisotropy.

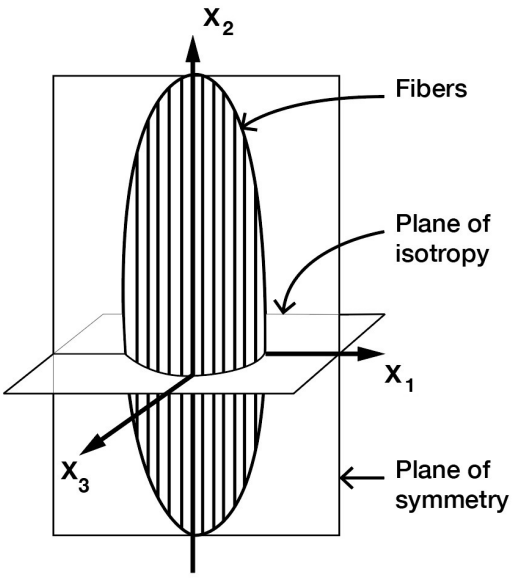

Figure 5: Schematic view of a tissue sample characterized by transverse isotropy. Credits to D. Klatt.

Let u_0 be the initial displacement amplitude, $\vec{n}$ the vector normal to the wavefront, $\vec{r}$ the coordinate vector $(x_1, x_2, x_3)^T$, the wave number $k = \frac{\omega}{c_s}$, $\vec{e}$ the unit vector in the displacement direction, then a shear wave can be considered,

$$\vec{u}(\vec{r}, \omega) = u_0 \exp\left(-ik\vec{n} \cdot \vec{r}\right)\vec{e}_{\perp\vec{n}} \tag{4.4}$$

the direction of displacement is perpendicular to the propagation direction. Considering an elastic linear isotropic material (and homogeneous) and plugging the wave equation into the

general Navier's equation with no body forces applied, the shear wave speed can be computed as

$$c = \sqrt{\frac{\mu}{\rho}} \tag{4.5}$$

as previously introduced in Equation 1.6.

On the other hand, for longitudinal waves,

$$\vec{u}(\vec{r},\omega) = u_0 \exp\left(-ik\vec{n}\cdot\vec{r}\right)\vec{e}_{\|\vec{n}} \quad , \tag{4.6}$$

the wave propagation direction is parallel to the direction of oscillation and the compression wave speed is expressed as

$$c = \sqrt{\frac{\lambda + 2\mu}{\rho}} \quad . \tag{4.7}$$

Elastographic displacement data need to be processed using motion equations that relate tissue response to tissue mechanical properties. Numerical algorithms have been developed to determine the complex shear modulus, which either use direct solution of motion equations or finite element model based simulations [14].

The complex (dynamic) modulus is composed of a real part (*storage modulus*) which gives information about the ability of the material to store elastic energy, and an imaginary part (*loss modulus*) which is related to viscosity and to energy dissipation [48].

The *complex shear modulus* (dynamic modulus) is the viscoelastic material property defined as the ratio of stress to strain under vibratory conditions. In such materials rheological models can

describe the stress-strain relationship over a wide frequency range. Here the springpot model is an accepted rheological model to describe the increase of the complex shear modulus with frequency with biological tissues [51].

Due to the geometry of the sample, interfering waves may be present and in such case MRE data can result in artifacts in the inversion algorithms. The *directional filtering* technique was developed to avoid such artifacts by separating waves propagating in different directions through the analysis of both temporal and spatial information [49].

Compression waves in MRE may jeopardize the computation of the viscoelastic shear properties of tissues. Since shear and longitudinal wave speeds differ in order of magnitude, the simultaneous solution of the wave equation for both Lamé constants is impractical due to the long compression waves. The component of longitudinal motion is typically removed from MRE data by applying the curl operator to the displacement field. This calculation involves discrete differences and therefore may increase noise contribution. It also requires three dimensional measurements of motion in all the three Cartesian directions, usually requiring long acquisition times. A valid alternative (even though less effective) to the exploitation of the curl is to employ a high-pass filtering, since compression wavelengths are much longer than those of shear waves. This filtering technique can be applied also to those datasets which do not share the comprehensiveness required by the curl operation (such as data with only 1 MEG direction or scalar displacement in 2D). For such 2D datasets, an implicit assumption is made that the shear wave propagation normal is parallel to the 2D image slice.

This assumption holds for ex-vivo studies performed in this dissertation. The wave equation after the application of the Curl operator is given by

$$\mu \nabla^2 \vec{u} = -\rho \omega^2 \vec{u} \tag{4.8}$$

Considering soft tissues with viscoelastic properties and thus attenuation characteristics, the complex shear modulus $G(\omega)$ is a function of the applied vibratory frequency rather than a constant. Therefore also the phase velocity and the damping coefficient of the shear waves are frequency-dependent

$$\begin{aligned} c(\omega) &= \frac{1}{\Re(\sqrt{\frac{\rho}{G(\omega)}})} \quad , \\ \gamma(\omega) &= -\omega \Im(\sqrt{\frac{\rho}{G(\omega)}}) \quad . \end{aligned} \tag{4.9}$$

Finally the solution of the shear wave equation is given by

$$\vec{u}(\vec{r}, \omega) = u_0 \exp\left(-i[\Re(k) + \Im(k)]\vec{n} \cdot \vec{r}\right)\vec{e}_{\perp \vec{n}} \quad . \tag{4.10}$$

Under the hypothesis that the tissue exhibits only a modest amount of attenuation (and so it can be considered as elastic), $c(\omega)$ can be used to compute the shear modulus as in Equation 1.6. If geometrical focusing is considered, an harmonic motion in a cylindrical test tube is assessed and using boundary conditions on a cylindrical conditions, $u_z = u_{za} e^{i\omega t}$, where u_z is the vertical displacement, u_{za} is its corresponding amplitude, ω and t are the displacement frequency and time, so the model creates shear waves propagating radially towards the center of the cylinder.

When a viscoelastic isotropic tissue is considered, the cylindrical coordinate wave equation provides the displacements as a function of the radius:

$$u_z(r,t,k_\beta) = u_{za}\frac{J_0(k_\beta r)}{J_0(k_\beta a)}e^{i\omega t} \quad , \tag{4.11}$$

where $k_\beta = \omega\sqrt{\frac{\rho}{\mu_R + i\mu_I}}$ is the surface wave number and $J_0(z)$ the Bessel function [51].
For isotropic and transversely isotropic materials and tissues, the profile lines crossing the center of the sample can be used to estimate $G(\omega)$ at different frequencies by matching the analytical closed form solution. Furthermore, complex shear moduli can be fitted to rheological models if MRE is performed at multiple frequencies.
For the investigation in MRE experiments of small tissue samples, the vibration frequencies needs to be $10-20$ times higher than those used in human MRE [52] so the attenuation of the complex shear modulus prevents immediate comparisons of data at different frequencies.

Studies of another group using the 0.5 T MRI system employed in this project, reported average values of the complex shear moduli of porcine muscle in the range 500 to 1000 Hz to be 9.55 ± 0.90 kPa for the storage modulus (the real part) and 2.06 ± 0.29 kPa for the loss modulus (imaginary part), while the values of porcine liver were 2.67 ± 0.76 kPa and 1.00 ± 0.21 kPa for the storage and loss modulus, respectively [8].

CHAPTER 5

MATERIALS AND METHODS

A benchtop MRI scanner constituted of a 0.587 T permanent magnet and a driver console was employed and further customized by adding an external gradient amplifier and an integrated custom-build piezoelectric actuator system of note. The whole system is represented in Figure 6.

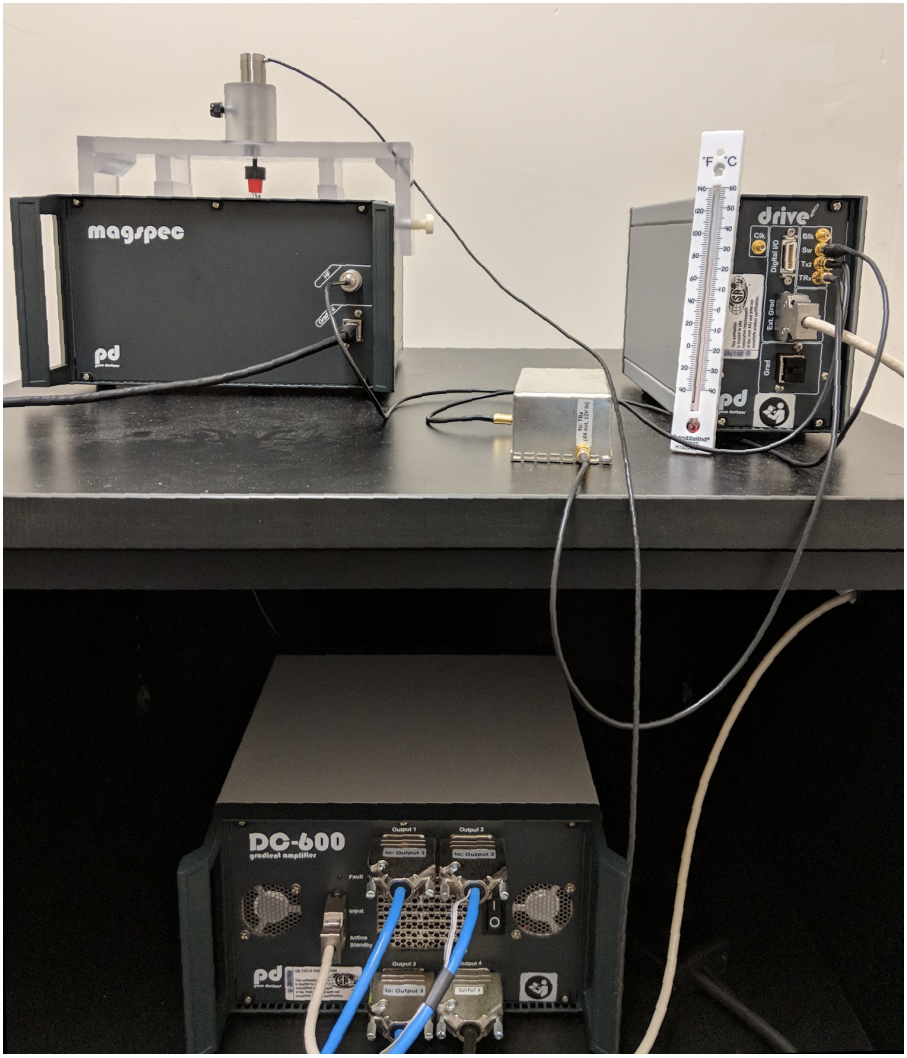

Figure 6: The system is comprised of a 0.5 T magnet (top left) with both the piezo-actuator support and the actuator mounted on it, a driver (top right) and a gradient amplifier (bottom).

Besides the presented hardware, a custom-designed piezo-actuator support was developed (Figure 8), so that the magnet, with such support, appeared as in Figure 7. A similar setup has already been used for the assessment of viscoelastic properties in animal tissue samples [8] and for the study of formalin fixation effects on biological tissue viscoelasticity [53].

Technical data of the employed instrumentation is described in the following Sections.

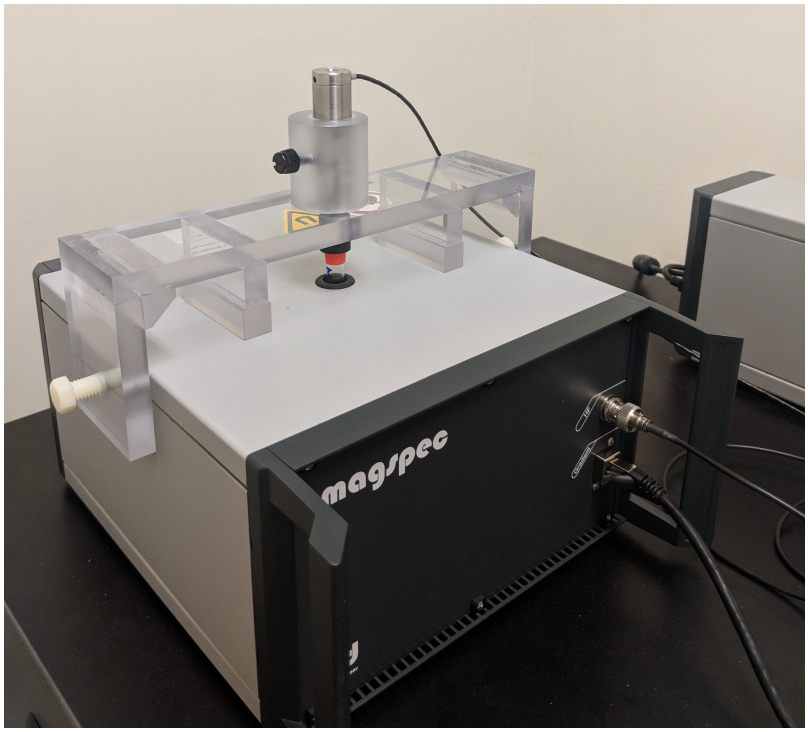

Figure 7: The 0.5 T magnet with both the piezo-actuator support and the actuator itself.

5.1 MRI scanner and setup

The Magnetic Resonance tomograph ResearchLab is constituted by different components which are here presented. The benchtop scanner (Pure Devices GmbH, Würzburg, Deutschland) was first installed and assembled with all the setup components, which comprises a physical driver, a low-noise pre-amplifier and switch, and a high-power external gradient amplifier (DC 600, Pure Devices GmbH, Würzburg, Deutschland). Also, a RJ-45 pre-calibrated adapter is used to connect the amplifier to the standard gradient system of the magnet. The MR scanner presents an ordinary system of reference whose y-axis is along the test tube (and bore) axis.

In general, a resonant circuit can be tuned to the nucleus frequency that has to be investigated and matched to the nominal impedance of the connecting lines, that is usually low (around tens of Ohms). This procedure is usually performed by adjusting two variable capacitors that are present in the circuit, so that by tuning and matching the quality factor and the dissipated power should reduce, leading to better sensitivity and shorter pulse widths [54]. Tuning and matching of this particular coil is performed on production of the magnet, since no varactors but rotary capacitors are used. A Network-Analyzer function is provided for cases in which a malfunctioning suspect is raised.

Being a Magnetic Resonance device, static magnetic field safety guidelines are provided and they suggest that people using devices for cardiac assistance and pregnant women should maintain a safety distance of 1 meter to the magnet and under no circumstances those persons may enter the 5 G (0.5 mT) line. The 5 G isosurface is found approximately at 0.6 m from the center of the magnet (better assessed with a magnetometer).

The ICNIRP states that the upper limit of magnetic field intensity that shouldn't be exceeded is:

- 40 mT for general population;
- 100 mT for place of employment;
- 3 mT for ferromagnetic implants and materials.

The benchtop system requires a working and licensed version of MATLAB (MathWorks, USA) not older than Version 2012a. The whole system is completely programmable with the MATLAB software and comes with a package of functions already implemented by the manufacturing company, which makes it ready-to-use.

In order to perform elastography-based studies, the piezoelectric actuator connector (Section 5.2) needs to be plugged into the RJ-45 adapter. Limitations are reported for all the output pins that are present on the interface of the external gradient amplifier and in particular, voltages over 30 V must be avoided. This voltage should be kept in mind in order to properly choose the desired displacement range for the piezoelectric element according to its relative calibration curve.

TABLE I: MAGNET FEATURES

Magnet magspec	
Static field intensity	0.587 T
^{1}H Frequency	24.99 MHz
Field homogeneity (5 mm)	<3 ppm
Field homogeneity (10 mm)	<30 ppm
Dimensions	27 cm × 25 cm × 14 cm
Weight	18.0 kg

The ROI of the benchtop MR device corresponds to the inner diameter of the test tubes, which is 8 mm. In order to adequately acquire shear waves within the sample and compute shear modulus in the transverse plane, with respect to the test tube axis, frequencies need to be chosen so that at least two wavelengths should be clearly visible in MRE phase images. For shear waves speeds around 1-10 m/s, frequencies should be

$$f > \frac{c}{\lambda} \tag{5.1}$$

where $\lambda < ROI_{length}/2$ that for the discussed device is $\lambda < 4$ mm. This leads to $f > 250$ Hz assuming $c = 1$ m/s in order to see at least a wavelength in the sample (considering the smallest wavespeed).

TABLE II: PIEZOELECTRIC ACTUATOR FEATURES

Piezoelectric actuator PAHL 60/20	
Displacement range (-10% +20%)	$64\mu m$
Capacitance ($\pm$ 20%)	$21\mu F$
Resonant frequency	$8KHz$
Stiffness	$8N/\mu m$
Preload	$350N$
Operating voltage	$-20V \div +130V$
Diameter	$20mm$
Length	$72mm$

5.2 Piezoelectric actuator and support

The PZT-based ceramic piezoelectric actuator (Piezosystem Jena, Jena, Germany - Table II) was employed in dynamical mode for MRE experiments, for which it was fed with a sinusoidal AC with a peak voltage of 30 V (corresponding to the highest output voltage of the gradient amplifier). The desired displacement range was chosen according to the calibration curve provided with the piezoelectric element, resulting in a maximum displacement of around 6 μm. According to its datasheet, the actuator should be used in a frequency range up to 80% of the resonance frequency, leading to a maximum frequency of 6.4 KHz [55].

The support has been fabricated in multiple polycarbonate pieces then chemically bonded together to ensure stability and accurate movements of the sample. The material was chosen for it being non-magnetic, for its high density, Poisson ratio ν and Young's modulus E which

would to prevent deformation when the piezoelectric actuator is turned on.

Eventually, a cap rod for the sample test tubes was also produced, so that a solid and stable connection could be achieved by screw it into the the M4-6Hx4 hole attached to the piezoelectric actuator sensible element.

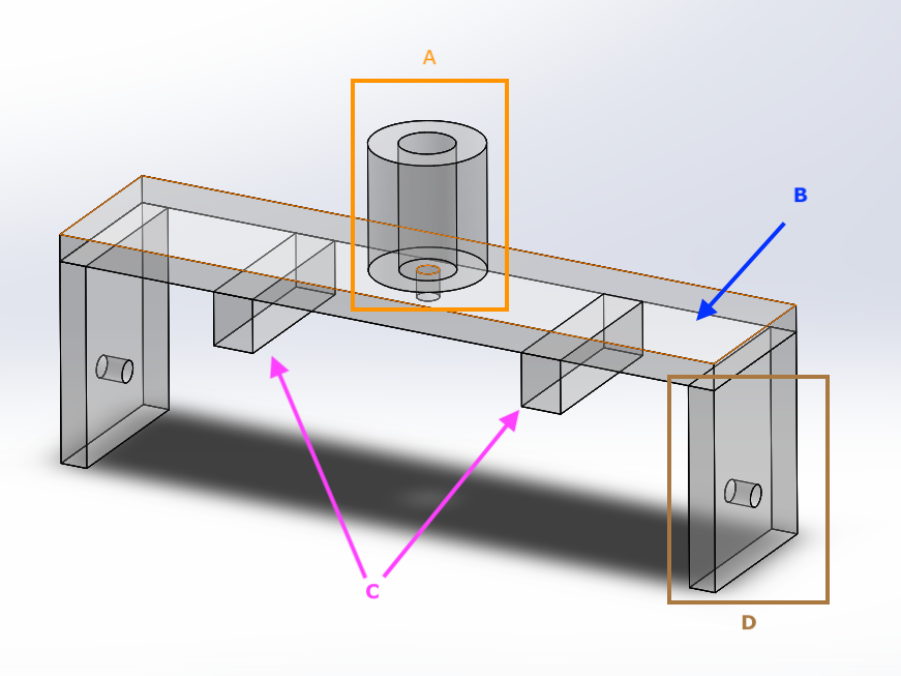

Figure 8: The piezoelectric actuator support has been realized in polycarbonate and its parts have been chemically bonded. This is the design concept. Part A hosts the actuator in its hole, with a H6 tolerance to ensure the lowest clearance. Part B represents the main dimension of the support, which is placed along the x-axis of the lab frame; in order to guarantee the highest inertia for harmonic displacement solicitations, the thickness of this part has been over-sized. Parts C were designed to lean on the magnet upper case face and to leave room for the cap holder and the upper part of the test tubes. Parts D presents screwed wholes to host flat-headed screws to tighten the support to the device. The real, modified, design presents additions to Parts C, two lateral joints and a screw in Part A for avoiding possible backlashes.

Its shape, dimensions and mechanical couplings have been designed in SolidWorks and successively adapted on the device itself to face an asymmetry problem (the bore of the magnet is not perfectly centered), tolerance issues and solidity enhancement: the cavity in the upper part of the support hosts the piezoelectric actuator, allowing a micrometric backlash since a H6 tolerance was chosen for fabrication.

5.3 Samples

Different samples were tested with the described setup:

- 6 samples of bovine muscle and 6 samples of bovine liver were acquired from the butcher as fresh meat, conserved at 4°C and then analyzed within the successive 48 h to avoid any impairment due to rancidification. Muscle samples were first carefully dissected so to assure the integrity of the tissue fibers along their predominant direction. Since transverse isotropy is assumed, muscle fibers should be oriented along the test tube axis, so to allow a correspondence between the plane of isotropy and the MR imaging plane (assuming transverse isotropy);
- 4 different MultiHance solutions at concentrations of 0.1 mM, 0.2 mM and 0.5 mM (below 1 mM, as for Section 2.2) were prepared from a commercial 0.5 M solution;
- 10% 15% and 20% weight over volume gelatine samples;
- A distilled water and a vegetable oil sample were used for shimming the device before every sequence acquisition.

For a smoother and easier insertion of the tissue samples inside the test tubes, these were professionally cut at the closed end: samples were inserted through the cut end and moved through the test tubes so to reach the Field Of View (FOV) of the device applying negative pressure at the opposite end of the tube (Figure 9). Tissue sample preparation was performed starting from bulk pieces and choosing a cut direction to preserve fiber direction in the anisotropic materials (muscle samples), and to orient the fibers parallel to the longitudinal axes of the glass test tube. To provide further stability and don't allow the samples to run down in the test tube, a 20% weight over volume gelatine was poured from the cut end of the test tube. In order to preserve tissue properties, gelatine was placed in contact with the bottom part of the tissue sample but far from the FOV.

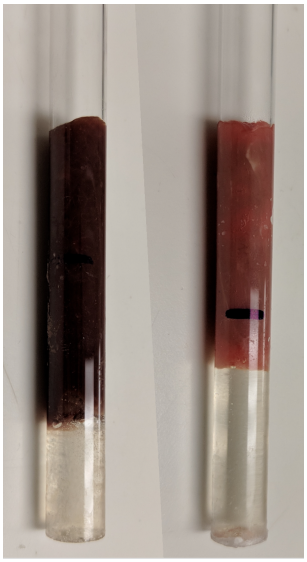

Figure 9: Liver (on the left) and muscle (on the right) samples. Gelatine is placed below the tissue in order to avoid any sliding of the sample itself. The blue line represents the bottom end of the FOV.

Although a slice selection code line can be exploited in the imaging sequences, for a precise calculation of the height at which the sample should be placed inside the test tube a few facts should be known: a support tube is found within the device, and the center of the FOV is about 45 mm above the bottom of the device, while the distance from the top cover is roughly 66 mm (Figure 10). Due to constructional inhomogeneities, the homogeneous region is not always the center of the magnet. The sensitive region has a height of about 11 mm, composed of the 10 mm coil size and the stray field part.

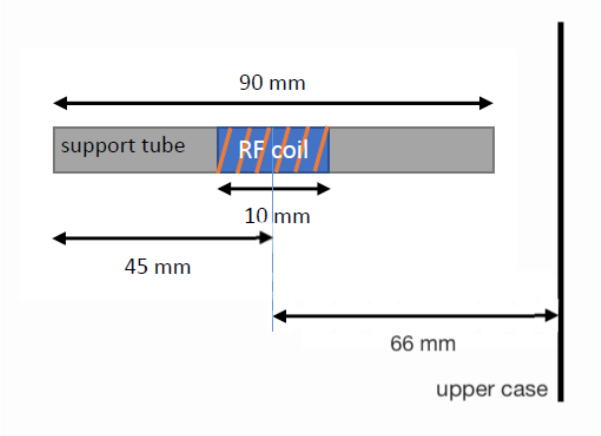

Figure 10: FOV of the system. An accurate positioning of the sample is needed.

5.4 Sequences

Prior to any assessment with the tabletop system, shimming should be performed by running a macro function. A general recommendation is to perform this procedure with a oil sample, since it shows a ten-fold shorter T_1 relaxation time with respect to a normal water sample (a typical T_1 of water is about one order of magnitude longer than the T_1 of a typical oil). Nevertheless, in a regime where the chemical shift is important, shimming with a water sample should be performed even though the optimization would take a longer time because the repetition time would have to be increased to the 10-fold to maintain a stable signal level.
Usually the chemical shift (3.5 ppm between oil and water [56]) is fairly low compared to the shift introduced by the imaging gradients and (for the most commonly used imaging sequences) leads to very minor deviations, mainly a small translation of the k-space in the read encoded di-

rection corresponding to a linear phase in image space, so for imaging purposes at low-intensity magnetic field intensities chemical shift may be neglected.

5.4.1 Relaxation times determination

The determination of both T_1 and T_2 relaxation times was performed by exploiting built-in functions of the benchtop system. In particular, the longitudinal magnetization signal was automatically reconstructed after an inversion recovery sequence for the computation of T_1, while the transverse magnetization signal was automatically reconstructed after a stimulated-echo sequence. Since the aim of both computations was to obtain relaxation time values for the whole sample within the ROI, the image slice corresponded to the whole 10 mm within the RF-coil region shown in Figure 10. Also, expected values needed to be inserted to correctly estimate the relaxation times.

For the T_1 an inversion recovery sequence is provided and the behavior of the longitudinal magnetization is automatically reconstructed, for a duration that is set on a user-estimated T_1 (which should be close to the real T_1 to allow convergence of the automatically exploited fitting algorithm). With a $TR = 5 \cdot T_{1,expected}$, an averaging of 50 signals, each one measuring 20 FIDs, is performed to decrease noise contribution and based on the time-varying signal a logarithmic transformation is applied. The longitudinal relaxation time was algebraically computed as the sign-changed inverse slope coefficient of the linear fitting between the time vector and the logarithmic transformed signal whose values were computed as

$$y = m \cdot x + q = \log \frac{\max M_z - M_{z,i}}{\max M_z - \min M_z} \cdot t + q \quad , \tag{5.2}$$

where $M_{z,i}$ is the modulus of the ith sampled value, $\max M_z$ is the maximum of the signal that is considered to be the longitudinal magnetization intensity at equilibrium condition and $\min M_z$ is the minimum of M_z that corresponds to the first value of the acquisition after the RF-pulse application. To graphically visualize the signal and evaluate the expected exponential behavior, the computed T_1 was plugged into Equation 2.2.

Similarly, the computation of T_2 is carried out by providing a stimulated-echo sequence to the sample. Also for T_2 computation, $TR = 5 \cdot T_{1,expected}$, 50 signals were averaged, each one measuring 20 FIDs and a logarithmic transformation of the trasverse magnetization data was applied, so to compute the trasverse relaxation time as done for T_1. In this case the logarithmic signal was computed as

$$y = m \cdot x + q = \log \frac{M_{z,i}}{\max M_z} \cdot t + q \quad , \tag{5.3}$$

and data were plotted as in Equation 2.2.

5.4.2 Diffusion MR sequence

A custom-made diffusion sequence using implemented macro functions defined in a MATLAB environment was developed as part of this project. The main purpose of this sequence is to compute the components of the diffusion tensor along its diagonal, through the application of x-, y- and z- directed gradients in order to assess an eventual isotropy of the analyzed sample. A spin echo sequence was upgraded with diffusion gradients. The complete diffusion can be found in Appendix A.

The time delay between the application of the RF-pulses and the gradients, namely the Δ value, was fixed. Echo Time and Repetition Time were $TE = 50$ msand $TR = 5000$ ms, respectively, so that a complete recovery of the longitudinal magnetization is achieved after the TR.

50 acquisitions per each b-value and per each gradient direction were averaged in order to increase SNR. To perform a variety of acquisitions at different b-values, the gradient amplitude was modified, thus increasing the b-value from 0 to 1400 s/mm^2. For this sequence the exponential decay signal and the echo signal were sampled at 30 kHz and the first value at b-value $b_0 = 0$ s/mm^2 was considered as a reference; for all the repetitions the maximum amplitude of the echo signal was evaluated and normalized to the value at b_0. The ADC value was then computed per each data point, while a more informative value was given by the slope of regression line in logarithmic scale fitted to the data.

5.4.3 MR Elastography sequence

A spin-echo MR acquisition is performed (the sequence was provided by the Berlin group, that is gratefully acknowledged). The sequence employs 3 RF-pulses $(\pi/2, \pi, \pi)$: while the first generates a transverse magnetization, the purpose of the second and the third refocusing pulses is the creation of the echo. A trapezoidal MEG was employed and the encoding efficiency for such gradient shape was computed. Considering a squared wave MEG that develops synchronously with a sinusoidal induced displacement, then sharing the same frequency and a null relative phase shift, the phase signal becomes

$$\phi(s) = \gamma \int_s^{s+\tau} K_0 sign\Big(sin(\omega t)\Big) Y_0 sin(\omega t) dt = 2\gamma \int_s^{s+\tau/2} Y_0 sin(\omega t) dt = \frac{4\gamma Y_0 K_0 q}{\omega} \quad . \tag{5.4}$$

The encoding efficiency is

$$\xi = \frac{4\gamma K_0 q}{\omega} \quad , \tag{5.5}$$

which is higher (factor $4/\pi$) than the encoding efficiency for a sinusoidal MEG.

Through the polarization of the vibrations within the test tube due to the constrained axial motion direction of the actuator, concentric cylinder waves were generated from the outer edges of the sample going towards its axis and so the motion field acquisition was limited to the uni-axial component, as in [53]. Vibratory frequencies higher than c/λ_{max} (determined by shear wave speed and sample dimensions) were employed: the frequency range went from 500 Hz to 2000 Hz and in order to avoid static phase offsets and to increase SNR, MEG direction was inverted at each second-wave image acquisition. 4 phase increments shift, spaced of $\pi/4$, were

employed. MEG amplitude and slew rate were 200 mT/m and 2000 T/m/s, respectively. For the minimization of phase discontinuities, 2D phase unwrapping relying on Flynn's algorithm was performed [57]. Successively, the complex wave images were calculated and then spatially filtered [8]. The Regions Of Interest (ROI) were either manually or automatically chosen through a MATLAB custom-made masking function, which detects the glass tube boundaries. For the computation of the complex modulus line profiles were matched with the Equation 4.11 (the analytical closed solution) per each frequency in a geometrical focusing condition of the surface waves. A MATLAB "Global Optimization"custom-made toolbox was employed to fit surface waves in a geometrical focusing condition. The algorithm minimizes the error function defined as the sum of the square of the distance between experimental data and Equation 4.11. The required inputs for the computation are the MEG frequency, the material density (which was assumed 1 g/cm^3 for every sample) and the gradient strength. After individual profile fit, an averaging of both shear modulus real and imaginary parts for the profiles at each frequency is performed and standard deviation is reported.

5.5 Statistical analysis

The estimations of the T_1 and T_2 times were averaged per each muscle and liver sample. Data of the same tissue type were averaged to obtain a unique informative value which was then compared with scientific literature data. Supposing data normality and unequal variances, a t-test for unpaired samples was performed to test the null hypothesis of equal population means. Data from diffusion sequences were preliminary analyzed and then ADC values (for isotropic samples) and Apparent Diffusion Coefficient values (for anisotropic samples) were computed for low values < 400 s/mm^2 as the slope of the regression line obtained through a minimization of sum of squared residuals. Comparison with the literature data is reported. T-test for unpaired samples were performed between each dataset related to each direction of the diffusion gradient. Furthermore, a t-test for MD values is reported.

Averaging of the complex shear modulus for each sample material (either gelatine or a specific tissue type) was performed at each employed frequency for the 4 acquired profiles. Analysis of the average and standard deviation for the real and imaginary part is performed, and the fitting error is calculated (see the next Chapter for details).

CHAPTER 6

RESULTS AND DISCUSSION

6.1 Relaxometry

Relaxation times were computed as the slope the data pertaining to the longitudinal magnetization. Data were sampled and fitted with a regression line after a logarithmic transformation, as discussed in Subsection 5.4.1.

From the relaxation times, the relaxation rates for MultiHance were computed and then normalized for the concentration of the considered sample in order to obtain the so-called relaxivity. Samples were analyzed in laboratory standard conditions.

Results per each concentration are shown in Table III and in Table IV.

For the longitudinal magnetization, the average relaxivity was 9.16 $s^{-1}mM^{-1}$ with a standard deviation of 1.77 $s^{-1}mM^{-1}$ ($n = 78$).

For the transversal magnetization, the average relaxivity was 11.49 $s^{-1}mM^{-1}$ with a standard deviation of 1.84 $s^{-1}mM^{-1}$ ($n = 84$).

A double tailed two-samples t-test with unknown variances and no assumptions was performed with the r_1 and r_2 values, giving a p-value $6.4e-14 << 0.05$.

TABLE III: MULTIHANCE LONGITUDINAL RELAXIVITY R_1 RESULTS - VALUES ARE REPORTED AS MEAN (ON THE LEFT) AND STANDARD DEVIATION (ON THE RIGHT) PER EACH CONCENTRATION

MultiHance Relaxivity r_1 per Concentration $s^{-1}mM^{-1}$							
0.1 mM		0.2 mM		0.5 mM		*weighted average*	
10.836	1.166	7.712	0.437	7.727	0.373	9.159	1.773
n=36		n=15		n=27		n=78	

TABLE IV: MULTIHANCE TRANSVERSAL RELAXIVITY R_2 RESULTS - VALUES ARE REPORTED AS MEAN (ON THE LEFT) AND STANDARD DEVIATION (ON THE RIGHT) PER EACH CONCENTRATION.

MultiHance Relaxivity r_2 per Concentration $s^{-1}mM^{-1}$							
0.1 mM		0.2 mM		0.5 mM		*weighted average*	
13.678	0.611	10.535	1.044	9.904	0.232	11.492	1.837
n=31		n=26		n=27		n=84	

Assuming that the muscle and the liver samples constituted two different groups (without accounting for the result of a one-way ANOVA test), both longitudinal and trasverse relaxation times for liver and muscle samples were computed. 6 samples were analyzed and 16 observation (averages of 50 signals) were computed for each tissue sample, both for the estimation of T_1 and for that of T_2. The averaged mean and standard deviation are reported in Table VI, as well as the values for each sample.

With respect to the mean literature values found in [38], data mean values are compared in Table V. As shown, all values are within σ from the mean value reported, except for liver T_1.

TABLE V: RELAXOMETRY VALUES [IN SECONDS] FOR MEAN T_1 AND T_2 FOR LIVER AND MUSCLE COMPARED TO SCIENTIFIC LITERATURE VALUES.

	Muscle			Liver	
	T_1	T_2		T_1	T_2
mean value	0.6098	0.0507	mean value	0.2185	0.0411
std	0.0081	0.0003	std	0.0031	0.0002
Muscle (Bottomley):	*0.5852*	*0.0470*	*Liver (Bottomley):*	*0.3451*	*0.0430*
σ inferior limit:	0.4799	0.0409	σ inferior limit:	0.2830	0.0370
σ superior limit:	0.6905	0.0531	σ superior limit:	0.4072	0.0490
2σ inferior limit:	0.3745	0.0348	2σ inferior limit:	0.2209	0.0310
2σ superior limit:	0.7959	0.0592	2σ superior limit:	0.4693	0.0550

An example of a T_1 and T_2 data fitting is found in Figure 11 and Figure 12. For each sample, a t-test for testing the hypothesis that the mean value of the T_1 is equal to the mean value of the T_2 of the same sample has been performed. When performed on the whole T_1 and

T_2 dataset for muscle and liver, p-values for both test resulted to be $p - value \ll 0.001$ (they were respectively $3.1 \cdot 10^{-162}$ and $1.5 \cdot 10^{-24}$). A boxplot of muscle and liver data distribution is reported in Figure 13.

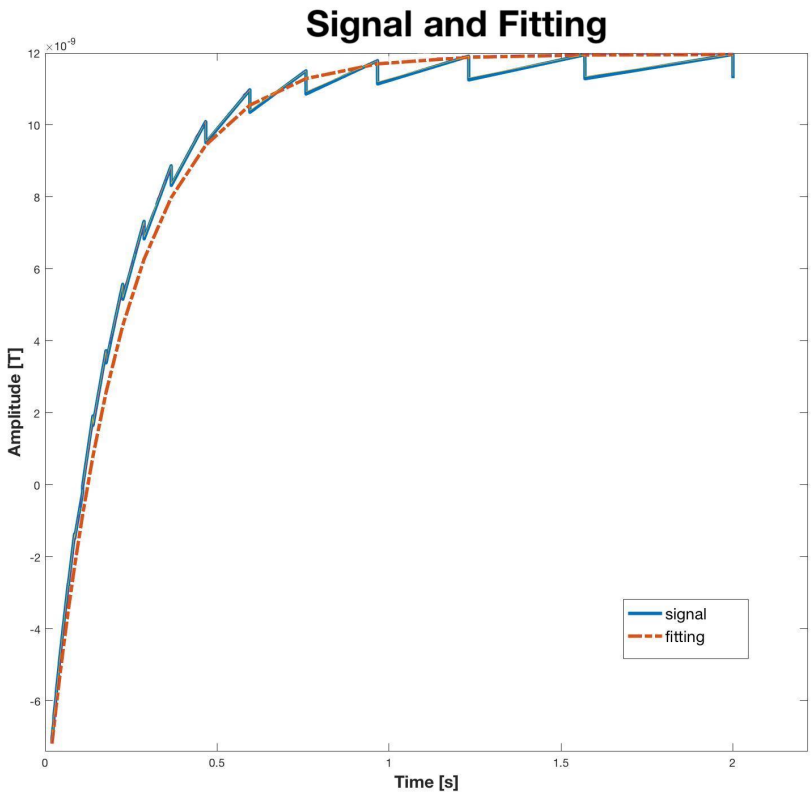

Figure 11: Example of Liver T_1 data fitting. Fitting was performed by considering only the maximum values of the sample groups (20 values are acquired in each 200 μs acquisition windows) and by considering the whole data set. Values on the vertical axis are in s^{-1}.

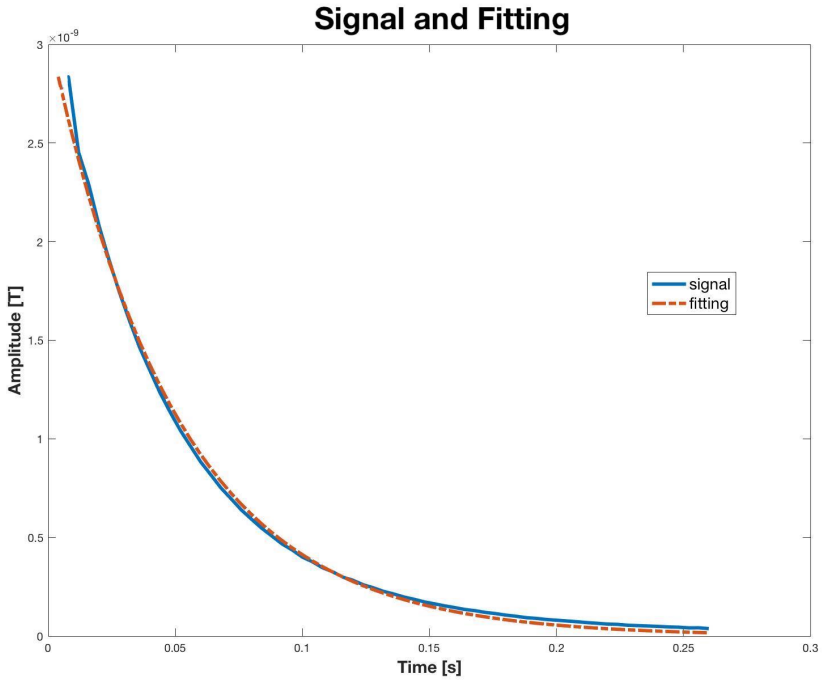

Figure 12: Example of Muscle T_2 data fitting. Fitting was performed by considering only the maximum values of the sample groups (20 values are acquired in each 200 μs acquisition windows) and by considering the whole data set.

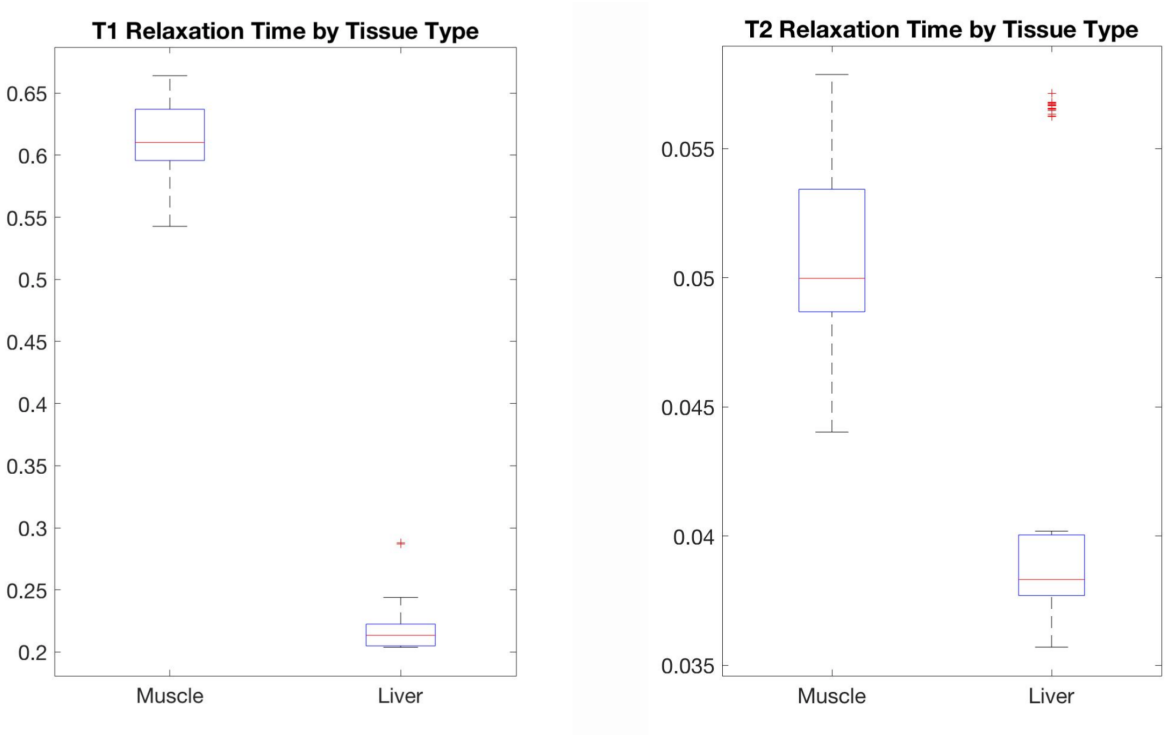

Figure 13: Boxplots for Liver and Muscle relaxation times. Values are in seconds.

A comparison of the obtained relaxation values with the literature models (relaxation rates against magnetic field intensity) was performed. In particular, models in [37] and [36] were considered, which described the relaxation rate R_1 as:

$$R_1(\omega) = A\omega^{-b} + C \quad , \tag{6.1}$$

where $A_{liver} = 17 \cdot 10^4 \pm 2.2 \cdot 10^4$, $b_{liver} = 0.58$, $C_{liver} = 0.35\ \mathrm{s}^{-1}$ and $A_{muscle} = 17 \cdot 10^4 \pm 2.2 \cdot 10^4$, $b_{muscle} = 0.6$, $C_{muscle} = 0.35\ \mathrm{s}^{-1}$. A plot showing the range of estimated values, following the

references, and the position of the computed values for both liver and muscle is reported in Figure 14 and Figure 15.

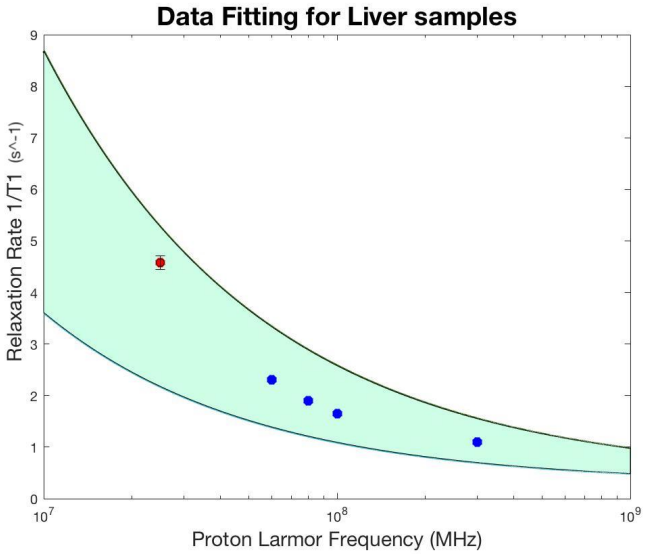

Figure 14: Liver R_1 found with the 0.5 T benchtop magnet are in red, while literature data from the quoted references are represented in blue. The shadowed area refers to the region computed considering the range for parameter A of the fitting. Values on the vertical axis are in s^{-1}.

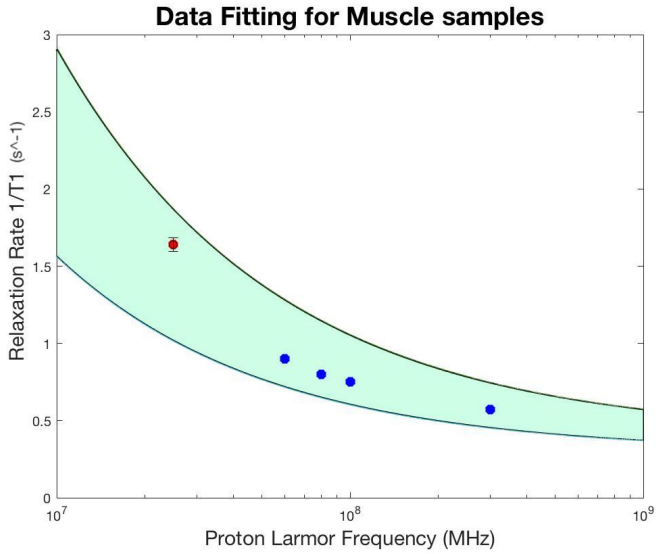

Figure 15: Muscle R_1 found with the 0.5 T benchtop magnet are in red, while literature data from the quoted references are represented in blue. The shadowed area refers to the region computed considering the range for parameter A of the fitting. Values on the vertical axis are in s^{-1}.

TABLE VI: RELAXOMETRY VALUES FOR T_1 AND T_2 FOR BOTH MUSCLE AND LIVER SAMPLES ($N_{OBSERVATIONS} = 16; N_{SAMPLES} = 6$). VALUES ARE IN SECONDS.

Relaxometry Summary for Muscle and Liver Samples

	Muscle				Liver			
	mean T_1	std T_1	mean T_2	std T_2	mean T_1	std T_1	mean T_2	std T_2
1	0.64091	0.01014	0.05751	0.00025	0.24811	0.01389	0.05651	0.00023
2	0.61800	0.0163	0.04943	0.00078	0.22372	0.00322	0.03871	0.00060
3	0.65557	0.00159	0.04957	0.00078	0.22109	0.00042	0.040005	0.00002
4	0.54472	0.00219	0.04999	0.00004	0.20907	0.00045	0.03575	0.00002
5	0.60336	0.01698	0.05344	0.00005	0.2049	0.00043	0.03823	0.00007
6	0.59614	0.00142	0.04409	0.00009	0.20412	0.00024	0.03770	0.00002
average	**0.60978**	**0.00810**	**0.05067**	**0.00033**	**0.21859**	**0.0031**	**0.04116**	**0.00016**

6.2 Diffusion MR

A representation of the diffusion MR sequence which was developed and can be found in Figure 16, while a signal output example is in Figure 17 and in Figure 18 a fitting example for the b-value against the logarithm of the signal intensity is shown.

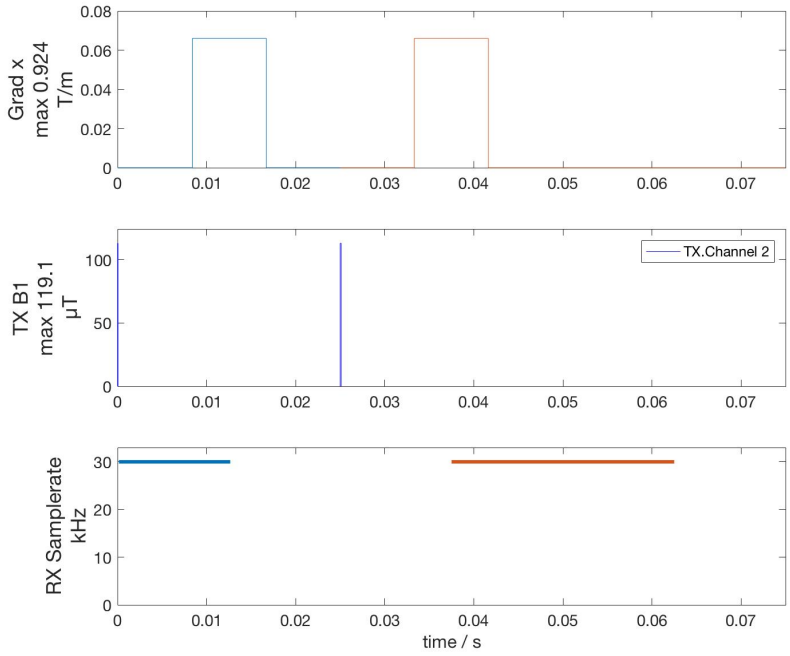

Figure 16: The custom-made diffusion sequence applies two successive RF-pulses $\pi/2$ and π as in a spin-echo sequence and the two diffusion gradients, for dephase and rephasing (as seen in the upper and middle window). The first acquisition window is right after the first RF-pulse while the second one is centered at twice the application time of the second RF-pulse (as in the lower window).
Timings are defined by the user, which should perform a T_2 estimation beforehand, so to insert such value in the sequence. The diffusion sequence is aimed at the computation of the diffusion tensor diagonal components.

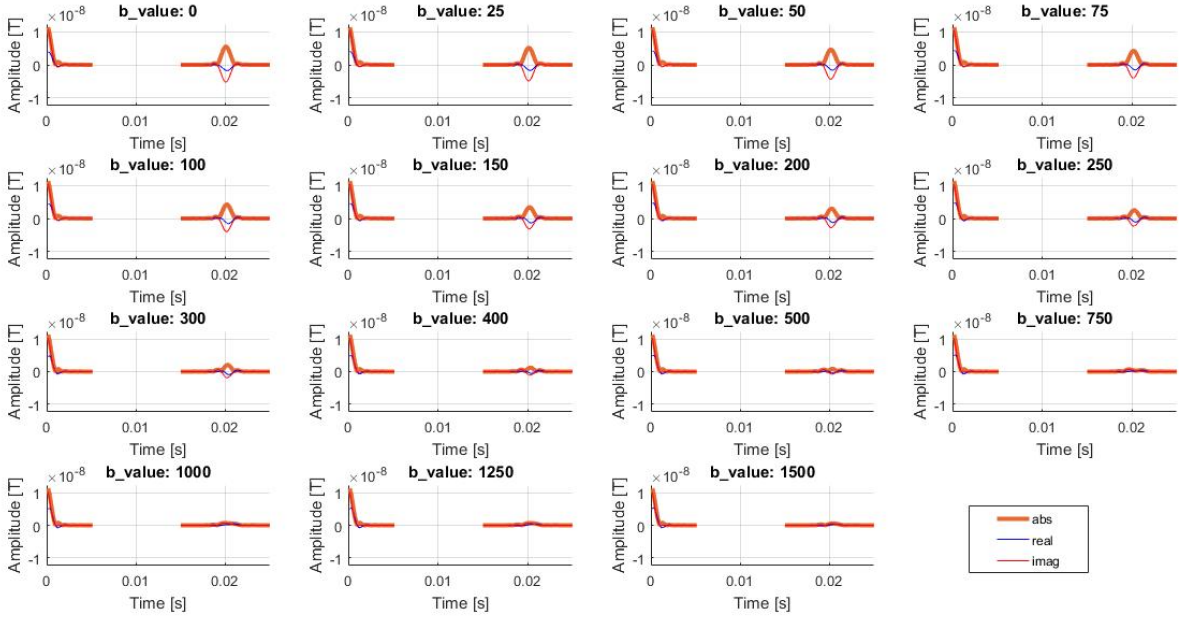

Figure 17: The output for the diffusion sequence shows a typical echo signal after the application of the refocusing 180° RF-pulse. For computing the values shown in Figure 18, the maximum of the echo signal is considered and then normalized with its intensity for $b = 0$ mm^2/s.

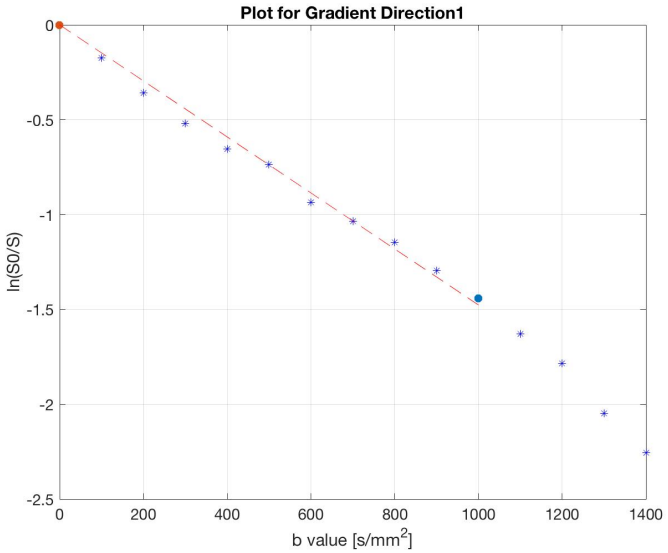

Figure 18: Fitting of the data for the computation of the first diffusion tensor diagonal component.

Diffusion properties were assessed for 12 gelatine samples (concentrations: 10% and 20% w/v, 6 samples each), 6 muscle and 6 liver samples (Table VII). Average MD values for the two gelatines, muscle and liver samples were 1.46, 0.99, 1.14 and 1.08 $\cdot 10^{-3}$ mm^2/s, respectively. Pair-wise Student t-tests were performed for the three orthogonal directions for all the samples and also for the MD average values for each sample type, as reported in Table VIII.

The range of b-values to employ in the analysis was selected after an exploratory analysis of the signal, which became distorted after a b-value (around 400 mm^2/s) that was set as the upper threshold for the computation of the regression line.

A significant difference ($p - value < 0.05$) was found for the diffusion gradient directions including the longitudinal axis in the muscle sample. Furthermore, MD values for the gelatine at 10% was found to be different with respect to all the other considered sample types.

No difference was found between the ADC components for the gelatines and liver samples, but also for the MD values among gelatine at 20%, muscle and liver samples.

TABLE VII: MEAN AND STANDARD DEVIATION VALUES FOR THE DIAGONAL ELEMENTS OF THE DIFFUSION TENSOR FOR ALL THE SAMPLES.

ADC components

values in $\text{x}10^{-3}\ mm^2/s$

		x-Direction	y-Direction	z-Direction	Average MD
Gel 10%	avg	1.42	1.53	1.49	1.46
	std	0.20	0.28	0.20	0.14
Gel 20%	avg	0.98	0.99	0.96	0.99
	std	0.12	0.19	0.24	0.10
Muscle	avg	0.92	1.65	0.90	1.14
	std	0.16	0.15	0.22	0.10
Liver	avg	1.06	1.06	1.15	1.08
	std	0.17	0.24	0.19	0.11

Number of samples = 6;
Averages per sample (NEX) = 4;

Literature values:

Muscle	$1.3 - 1.4\ \text{x}10^{-3}\ mm^2/s$
Liver	$0.7 - 0.8\ \text{x}10^{-3}\ mm^2/s$

TABLE VIII: STUDENT T-TESTS FOR ADC COMPONENTS AND MD AVERAGE VALUES FOR DIFFERENT DIRECTIONS AND DIFFERENT SAMPLE TYPES.

T-test
for ADC components
at different directions

	Dir. x-y	Dir. x-z	Dir. y-z
Gel 10%	0.39	0.48	0.77
Gel 20%	0.96	0.80	0.86
Muscle	**<0.001**	0.92	**<0.001**
Liver	0.76	0.33	0.27

T-test
of MD values
for different samples

Gel 10%			
<0.001	**Gel 20%**		
0.001	0.03	**Muscle**	
<0.001	0.22	0.33	**Liver**

6.3 Elastography

A firm piezoelectric actuator support in polycarbonate was successfully built so to make it steady during the actuator vibrations.

An example of the sequence employed for the determination of the mechanical properties through an elastographic approach can be seen in Figure 19. Data acquired by the sequence were then processed through a custom-made code which implemented all the steps for an MRE analysis which are:

1. Calculation of phase differences for the correction of static magnetic field inhomogeneities. Each acquisition is performed twice, with MEG "up"and "down"(toggled directions of MEG), and the two successive acquisitions are subtracted through a complex difference.
2. Correction of phase wraps in order to obtain the true phase accumulation. Flynn algorithm was employed for this aim.
3. Discrete Fourier Transform along time computed for each pixel over one period of vibration, which is subdivided in time steps, whose number has been chosen during the setting of the MRE sequence - the 1^{st} harmonic gives information about the energy of the wave.
4. Spatial Filtering to overcome the noise component.
5. Wave inversion for the computation of the complex modulus (through the "Optimization Toolbox").

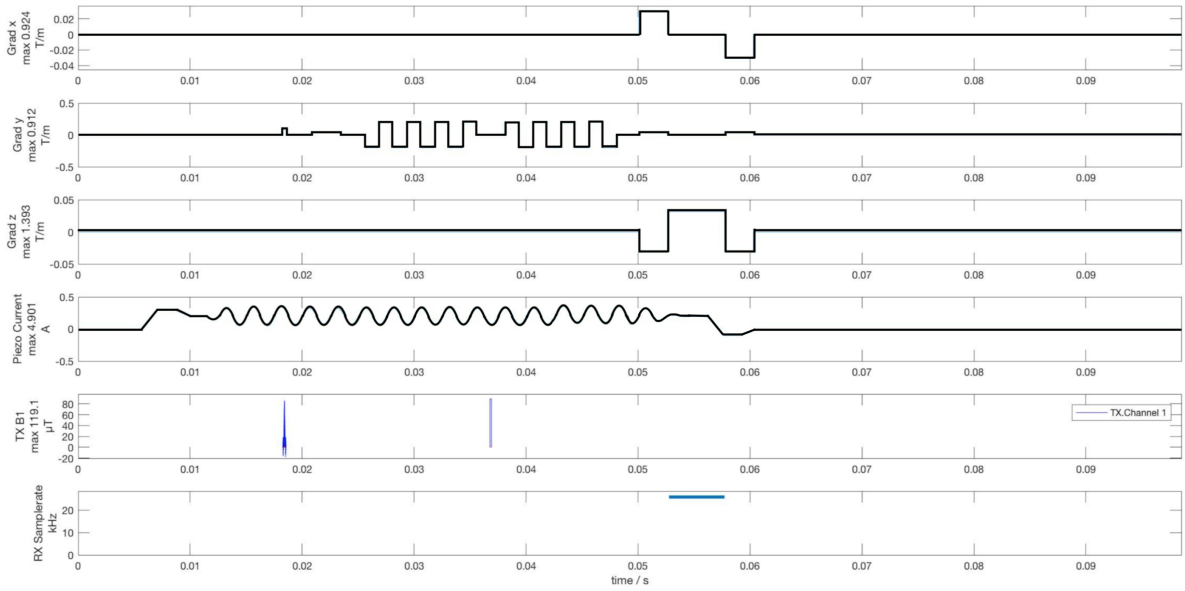

Figure 19: The MRE sequence shows the trapezoidal Motion Encoding Gradient along the y-direction, corresponding to the test tube main axis. The 90° (during the slice selection) and the successive 180° RF-pulse correspond to a standard spin-echo sequence, which leads to a rephasing of the signal, and to an echo which is sampled during the acquisition window. Data acquisition is performed between two gradient pulses along the x-axis whose inverse sign leads to a signal rephasing and while a z-gradient is on, so to perform contemporaneously a gradient frequency and phase encoding. The sequence was provided by the Berlin group, that is gratefully acknowledged.

For both the computation of the complex modulus and graphical purposes, a masking function was developed, which gives back a circular mask. An example of a mask and masked displacement image of a gelatine sample (excited with a MEG at 2000 Hz) is shown in Figure 20. The masking function allows the user to choose between selecting the center of the mask automatically or manually (in case the algorithm should provide an unreliable mask).

Sequence parameters for this analysis are found in Table IX.

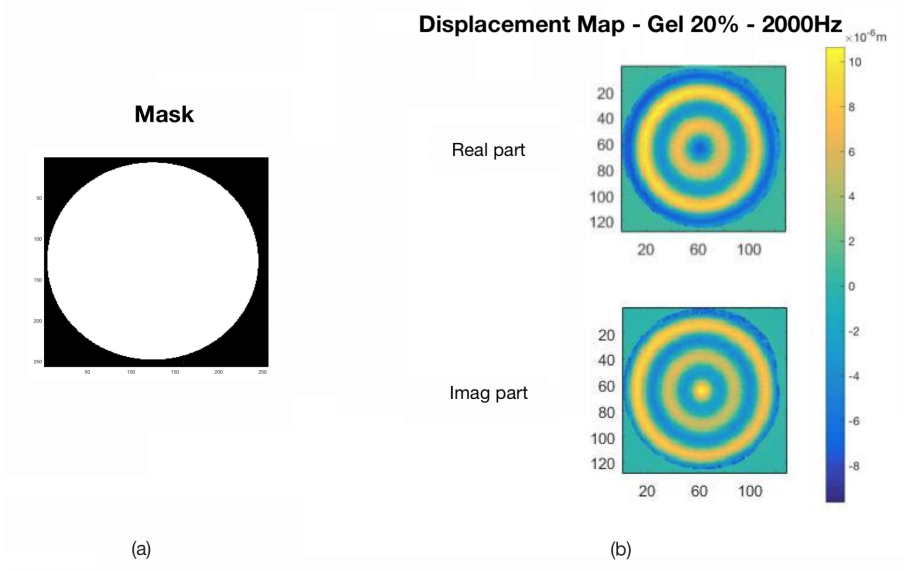

Figure 20: (a) A mask example from the masking function that was developed, which finds the center of the sample and, based on the dimensions of the test tube, finds the correct mask of 1 and 0 where 1 (white) refers to the ROI and 0 (black) refers to the external region.
(b) An example of real and imaginary masked displacement map for a gelatine 20% sample excited with a MEG (and acoustic frequency) of 2000 Hz.

TABLE IX: MRE SEQUENCE PARAMETERS - GIVEN THE TOTAL DURATION OF THE MEG CYCLES, MEG IS SYNCHRONIZED WITH THE VIBRATION FREQUENCY SO THAT AN INTEGER NUMBER OF CYCLES IS OBTAINED.

B0 [T]	Sequence type	MEG Amplitude [mT/m]
0.5	Spin Echo	200
MEG duration [s]	Averages	Vibration frequency [Hz]
0.02	5	500-2500

4 profiles per each frequency and sample were acquired and an estimation of both the storage and loss modulus (real and imaginary part of $G(\omega)$) was computed through MATLAB Optimization toolbox (iteratively changing the complex modulus in Equation 4.11 so to decrease the standard deviation of the data-fit distance) and the average of the complex modulus was weighted for the error (which is the summation of the square distance between the experimental data and Equation 4.11). The algorithm required the input of the expected parameter range in order to prevent instability of inversion. The limits imposed to the algorithm were such to preserve the waveform when a completely distorted one was chosen when trying to make an optimization of it. An example of the MATLAB Optimization tool is provided in Figure 21. Average values for the real and imaginary part and fitting error of the complex shear modulus for the several frequencies can be found in Table X. In particular, a graphical comparison between several gelatine concentrations is represented in Figure 22 while a comparison between liver and muscle properties against the 15% w/v gelatine sample are found in Figure 23 and Figure 24. The magnitude of the complex shear modulus is reported in Figure 25. Error bars define values within a standard deviation from the average.

TABLE X: VALUES FOR THE COMPLEX MODULUS FOR ALL THE SAMPLES. AVERAGE (AVG) AND STANDARD DEVIATION (STD) ARE REPORTED.

	Frequency	Gel 10%		Gel 15%		Gel 20%		Liver		Muscle	
	[Hz]	Avg	Std	Avg	Std	Avg	Std	Avg	Std	Avg	Std
Storage modulus [kPa]	500	5.39	1.55	9.55	1.07	9.79	1.00	6.49	1.53	24.73	6.60
Loss modulus [kPa]		2.62	0.62	2.31	0.40	2.50	0.41	4.22	1.41	5.11	3.50
Error		31.10	1.58	11.89	0.64	3.47	0.95	24.73	5.30	11.76	6.33
Storage modulus [kPa]	750	4.78	1.18	7.87	0.66	15.07	1.31	7.83	1.26	39.55	10.18
Loss modulus [kPa]		1.41	0.51	1.07	0.58	3.19	0.42	4.43	0.98	8.78	5.10
Error		30.28	3.26	17.48	1.37	7.52	1.57	40.05	3.17	10.62	3.94
Storage modulus [kPa]	1000	6.06	1.63	7.92	0.75	17.93	2.08	7.23	0.91	67.00	20.93
Loss modulus [kPa]		1.66	0.99	2.84	1.17	2.13	0.22	4.17	0.80	35.64	13.93
Error		31.40	7.84	28.91	1.72	19.70	0.59	35.81	5.85	9.49	2.71
Storage modulus [kPa]	1500	5.44	0.52	8.75	1.04	14.56	1.32	11.14	1.39	72.58	13.20
Loss modulus [kPa]		0.88	0.16	1.56	0.34	3.37	0.46	5.14	1.92	41.22	8.74
Error		36.88	2.37	28.61	2.48	20.13	0.40	44.24	4.12	14.73	3.10
Storage modulus [kPa]	2000	5.47	0.70	9.61	0.73	16.41	1.40	19.67	3.56	105.15	15.97
Loss modulus [kPa]		1.12	0.53	1.61	0.97	4.25	0.63	6.03	3.27	47.66	17.82
Error		24.58	3.20	30.42	3.50	9.03	2.34	48.14	4.12	18.76	7.93
Mean average error		30.85		23.46		11.97		38.59		13.07	
Mean std			1.78		1.16		1.01		2.64		9.33

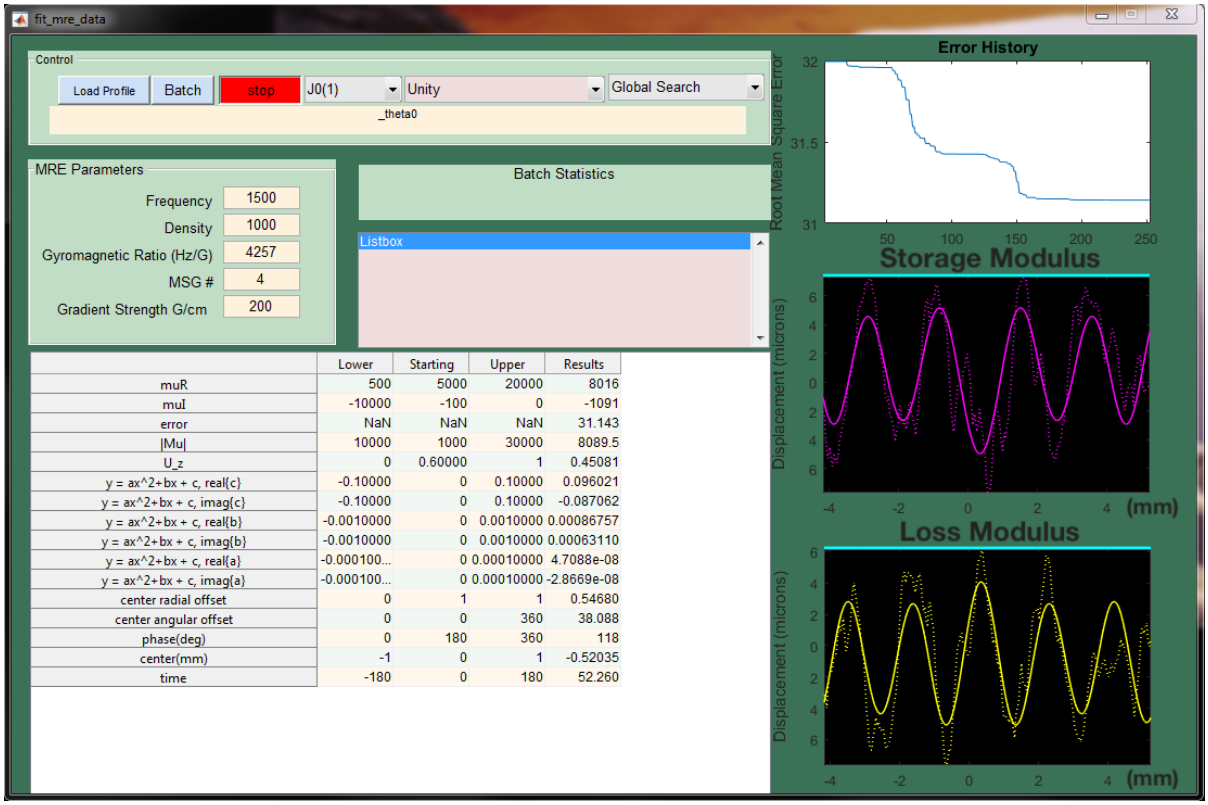

Figure 21: Graphic User Interface for MATLAB Optimization toolbox relying on Bessel fitting for a 15% gelatine. Storage and Loss moduli are estimated from an initial guess inserted by the user, spanning in a reasonable range of values also set by the user. On the right: profile data (dashed line) compared to the reconstructed real and imaginary displacement signal (continuous line) based on the guessed mechanical properties. It is possible to observe also the input window (top left) and the outcomes of the optimization in the "Results"column.

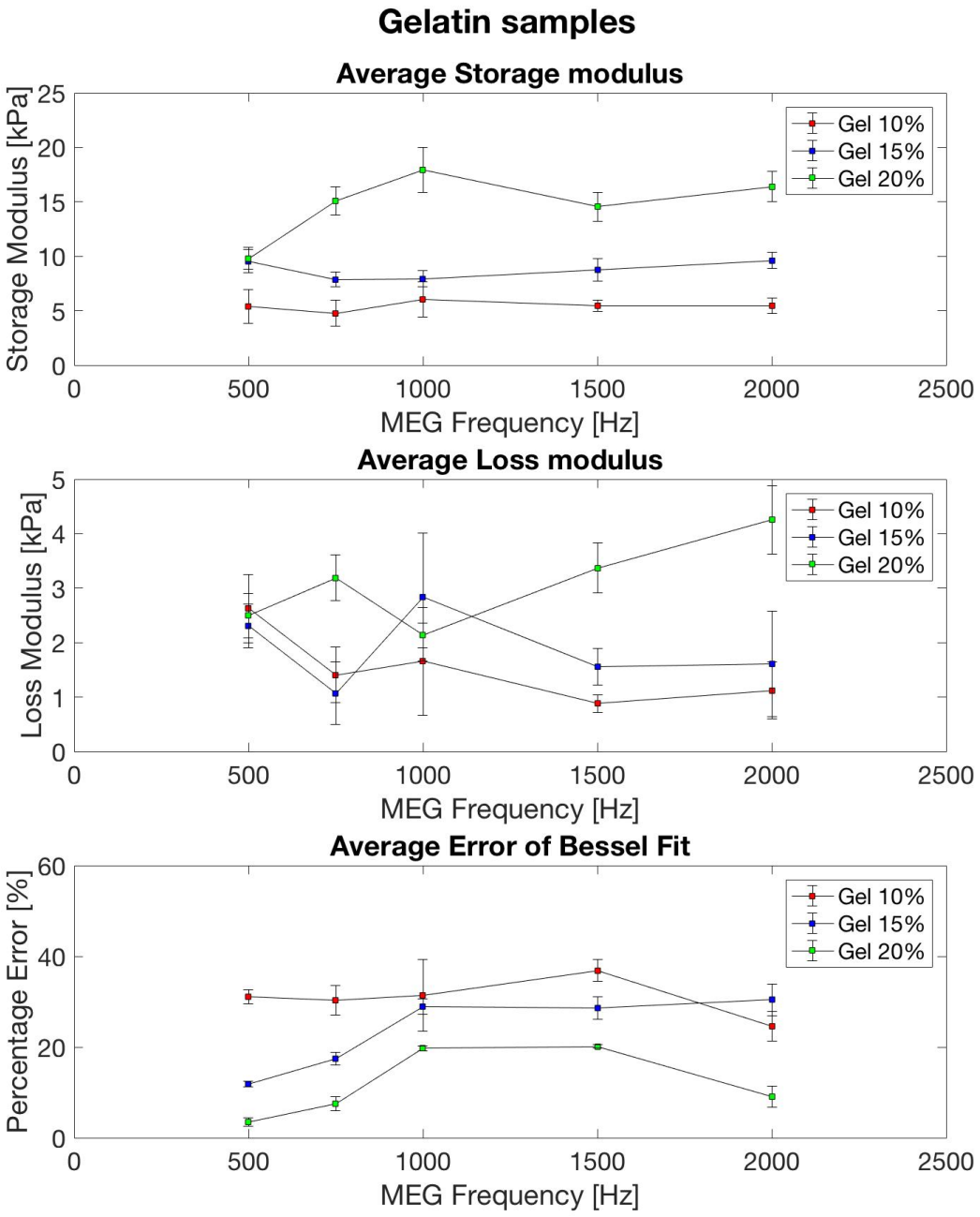

Figure 22: Storage and Loss modulus for different gelatine concentrations.

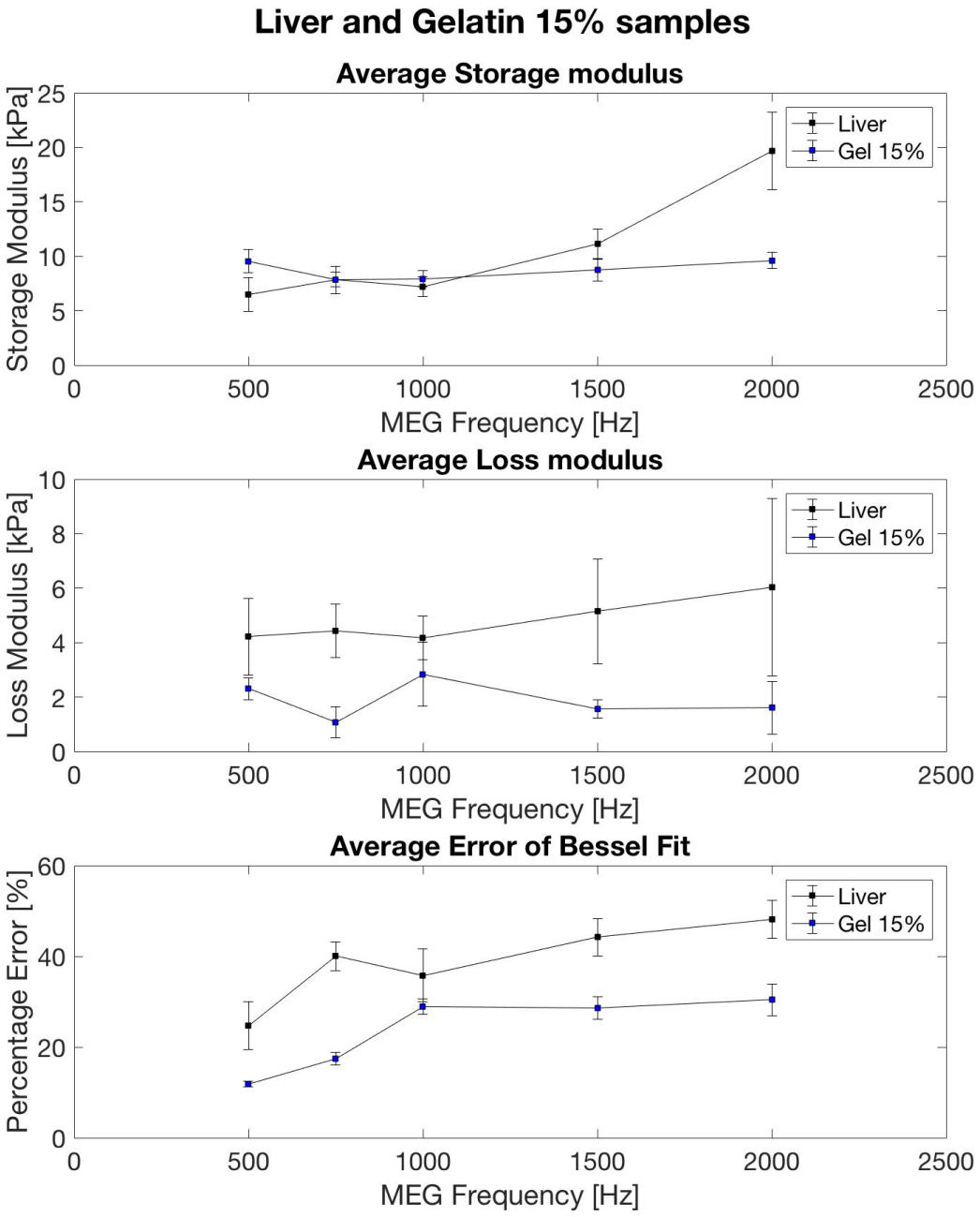

Figure 23: Storage and Loss modulus for liver and gelatine samples.

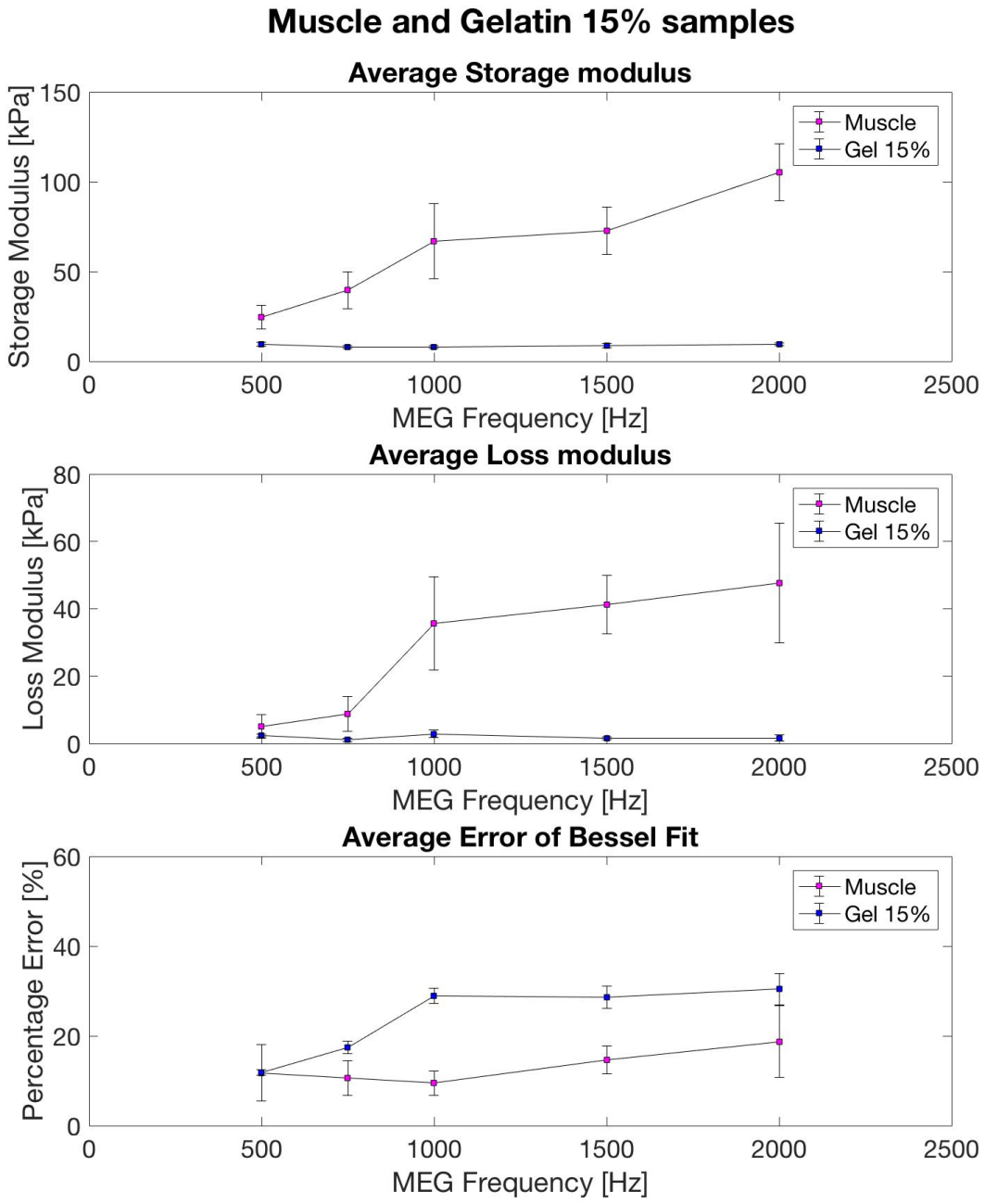

Figure 24: Storage and Loss modulus for muscle and gelatine samples.

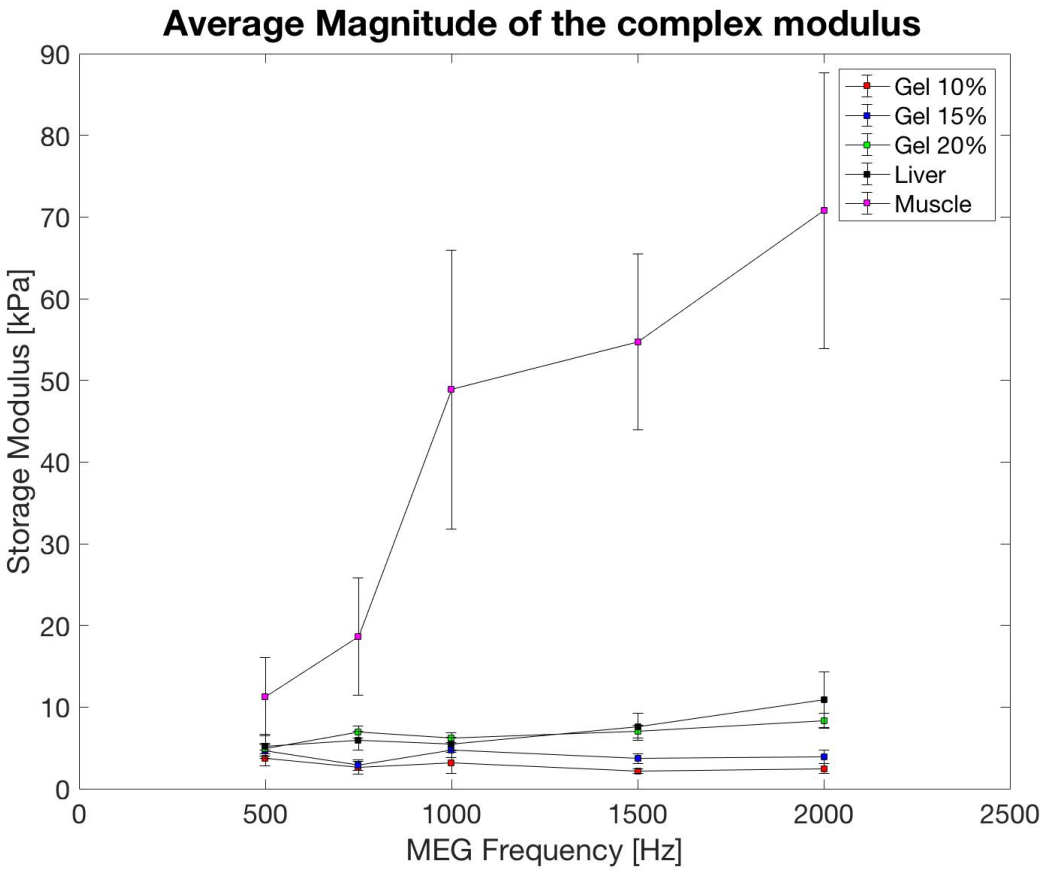

Figure 25: Complex shear modulus magnitude averaged over all samples.

Average storage modulus and loss modulus for liver samples increased clearly with frequency (from 6.49±1.53 to 19.67±3.56 kPa).

The values for muscle complex modulus were substantially higher than the values for all the other samples, with an increasing trend with frequency, so that a difference of an order of magnitude below 1500 Hz and a difference of two orders of magnitude above can be seen. Also, standard deviation for such samples is much higher than those of the other samples. Gelatine samples showed a slight increase of the average storage shear modulus with frequency while a clear increase of the storage shear modulus with increasing concentration can be assessed. The 20% w/v gelatine sample showed the lowest values of error and average standard deviation (1.01 kPa).

CHAPTER 7

CONCLUSIONS AND FUTURE DEVELOPMENTS

Magnetic Resonance at low-intensity field have only a few applications to the imaging field thus far. The use of low-intensity field scanners would allow lower price and operational costs and lower SAR within particularly sensible samples. Also, small low-intensity field scanners could be easily placed and shielded within clinical facilities and would be helpful for the analysis and imaging (with lower artifacts impact) of small samples, as usually the magnet bore dimension is considerately lower for low-intensity magnets (for a good detection of the signal). The present dissertation reported an analysis of either animal tissues and water-based solutions samples carried out with a benchtop 0.5 T scanner, both for a characterization of those samples through the most commonly used relaxation and diffusion parameters, and with also an elastography-based approach. Since the system is completely programmable through MATLAB code, a high level of usability and hands-on experience, as well as a good amount of reverse engineering know-how, was gained.

This project mainly concerned three aspects:

- The computation of relaxometry parameters for contrast agent solutions, gelatin, bovine liver and muscle samples through a linear fitting of the logarithm of the signal, thus providing a single exponential estimation of the signal.

- The development of a diffusion sequence and the computation of the Apparent Diffusion Coefficient (intended as the Mean Diffusivity) coeffiecient for gelatin, liver and muscle samples.
- The construction of a physical support for the piezo-actuator and the creation of an algorithm for the computation of the complex displacement maps from the magnetic resonance signal, for then computing the complex modulus for gelatin, liver and muscle samples.

Relaxometry data of solutions of the clinically used contrast agent MultiHance shown a transversal relaxivity value of 11.49 ± 1.84 $s^{-1}mM^{-1}$, different from the longitudinal relaxivity of 9.16 ± 1.77 $s^{-1}mM^{-1}$. The high value of relaxivity for water solutions of MultiHance, which come close to the values of such contrast agents in human blood plasma, can be related to the temperature dependence of relaxivity which was also shown for a static magnetic field of 7 T (as reported in Figure 2) that presents a maximum for a temperature around 300 K. It is reasonable to assume that even at lower magnetic field intensity a strong-temperature dependence of relaxivity may be observed, which could explain the results in this dissertation, which were found higher than the values expected from literature [27] that, on the other hand, were obtained at fairly different conditions including pH and temperature.

The variability of data given by its standard deviation then suggests that for a better computation of MultiHance relaxivity, a higher number of samples should be analyzed and more accurate standard procedure should be adopted, since successive dilutions (which were employed for sample preparation) may lead to mayor errors in the computation of a contrast agent relaxivity.

Values for liver and muscle relaxivity were found to be consistent with literature values [38] (except for the longitudinal relaxation time for liver samples) and were significantly different from one another. Muscle samples had a T_1 of 0.610±0.008 s and a T_2 of 0.051 s (and a standard deviation lower than 0.001) while liver samples had a T_1 of 0.219±0.003 s and a T_2 of 0.041 s (and a standard deviation lower than 0.001).

Moreover, the computed longitudinal relaxation times for both muscle and liver fit the model found in [37], which further validate the model at 25 MHz and provides a good reliability of such relaxation times at low-intensity magnetic field.

A diffusion MR sequence was developed from scratch and the signal was analyzed for the computation of a single ADC value for the whole sample.

The development of the sequence (reported in Appendix A) came with some challenges, such as the timing dependence of the whole sequence upon the T_2 time of the sample. A rapid decay of the signal after b-values around 1400 s/mm^2 was found for the orthogonal gradient directions belonging to the transversal plane. This behavior was also present in the longitudinal axis starting from even lower b-values (around 400-500 s/mm^2). For these reasons, the range of applicability of the sequence was restricted based on the diffusion gradient direction.

A difference was found between the average ADC components values for the transverse and longitudinal diffusion gradient direction in muscle samples (confirming its water motion anisotropy), whereas gelatines and liver samples didn't show any significant difference. Muscle and liver tissues had comparable values to the ones found in scientific literature [47], but not different from each other. Furthermore, the 10% gelatine was found to be the only sample to have

different diffusion behavior with respect to liver and muscle samples. This would suggest that the developed sequence is poorly sensitive and 20% gelatine would be suitable as a tissue-like phantom for liver and muscle tissues. The distortion of the signal over a certain diffusion gradient strength would suggest that a very simple diffusion sequence as the one that was herein presented isn't also able to compensate for the contribution of artifacts such as eddy currents, whose amplitude gets higher with higher gradient amplitude and slew rates since they are due to time-varying magnetic fields induced by gradient applications in the MR systems which lead to induced currents in the magnet components (as RF and gradient coils) which then result in unwanted magnetic fields [58].

Furthermore, all the steps for an elastographic MR analysis have been developed in a custom-made MATLAB code, which allows the use of a MRE sequence and acquire the complex displacement images.

Gelatin samples showed a slight increase of the average storage shear modulus with frequency while a clear increase of the storage shear modulus with increasing concentration was experienced. Gelatins at different concentrations showed a high reliability and fit of the displacement profiles with a low percentage error, which was substantially lower for the 20% w/v sample (11.97%). Liver and gelatin samples shared the same order of magnitude for the storage and loss modulus; the values regarding liver samples were found to be higher than the value reported in previous literature [8] for the analyzed range (around $6-7$ kPa in the range 500-1000 Hz for MEG frequency), as well as the values for the muscle tissues which exhibited very high values for the storage modulus (ranging from 24.73 to 105.15 kPa in the considered frequency range,

500-2000 Hz).

The increasing trend of the real part of the complex modulus with frequency in viscoelastic materials can be assessed in particular in liver (from 6.49±1.53 to 19.67±3.56 kPa) and 20% w/v gelatin samples (from 9.79±1.00 to 16.41±1.40kPa), but also for muscle samples, which had substantially higher values and standard deviations than those of all the other samples.

It may be suggested that the preparation of the sample may be critical for such tissue type, since air bubbles and detachment of the tissue from the glass test tube walls could result in incorrect stimulation and so inconsistent complex modulus values. A standardized procedure for tissue sample preparation able to avoid any air bubble presence should be developed.

7.1 Future developments

To conclude, further studies should be performed to assess the behavior of relaxation times, in order to choose the best time to perform ex-vivo relaxometry and diffusion experiments. Also, magic angle effect could be studied: when fibers lie at around 55°, T_2 gets longer, which leads to a corresponding increase in signal intensity, so by progressively changing the orientation of such tissues, the angular dependency of the relaxation times could be assessed.

The diffusion sequence here discussed and developed by the undersigned was found to be useful for the characterization of the muscle tissue and should be advanced and corrected for possible artifacts which may arise, such as the eddy current artifacts.

Being this a preliminary study, further investigations should focus on the optimization of all the processing steps, leading then to the development of T_1 and T_2 weighted imaging sequences, as well as to a more complete dissertation about diffusion tensors and tractography for this low

field intensity device. Also, results coming from MRE analysis should be compared with finite element models and rheological models and a validation with a standardized samples (with well-known complex modulus behavior over frequencies) could be beneficial. Further possibilities would be to compare the complex modulus values with analogous samples analyzed at higher field or even improving the accuracy of the estimation computed through the Optimization Toolbox by providing better masks and values for tissue density, increasing the number of profiles to be analyzed. Another possibility is to develop an optimization algorithm which could takes into account the preservation of the waveform besides the minimization of the squared errors.

Lastly, a higher number of samples should be analyzed in the future and different typologies of tissues could be employed to assess similarities and differences in terms of either relaxometry or diffusion or elastographic parameters at low magnetic field which may be of clinical importance, as already observed for liver fibrosis in the past.

APPENDICES

Appendix A

DIFFUSION SEQUENCE

Here follows the MATLAB diffusion sequence which was implemented for this project. Further details about the macro functions used herein can be found on Pure Devices (Pure Devices GmbH, Würzburg, Deutschland) website.

Appendix A (continued)

```
%% ADC computation
% SAMPLE AND B-VALUE SELECTION has to be performed before running this
% sequence. Also, remember to run the Auto_Parameter_Search function with
% an oil sample (or water sample) beforehand.
clear all, close all

Substance = 'Liver_May4';
Num_sample = 20;

Grad_direction = 1;

Estimated_T2 = 20e-3;

b_values0 = [0:50:400 500:150:1200]           % s/mm^2 (1 s/m^2 = 1e-6 s/mm^2
b_values0 = b_values0';
b_values = b_values0*10^6;                    % s/m^2, important for Gradient Amplitude

%%
n_signals   = length(b_values);
logs        = nan(n_signals,3)';
ADC         = [];
product     = [];
tot_col     = ceil(n_signals/4);
LoadSystem
[HW,mySave] = Find_Frequency_Sweep( HW, mySave,100);   % Find magnet frequency

gamma_cut   = 42.57747892*1e6;  % [Hz/T]
gamma       = HW.GammaDef;%2*pi*gamma_cut;
B0          = HW.B0;            % [T]

% Seq.ShimStart   =   [];
HW.Grad.x = 1;  HW.Grad.y = 2;  HW.Grad.z = 3;  HW.Grad.B = 4;
   % Assign gradient to output channel (optional)
HW.Grad.xyzBDir = [1,1,1,1]; % x y z B0 sign
   % Current direction (optional)
LoadCalcHW;
   % Calculate new hardware configuration

for Grad_dir = 1:3    %1:3
    for i=1:length(b_values)

        Seq.tRep        = [5 10]*Estimated_T2;
        Seq.average     = 2;
        Seq.averageBreak= 4*60*Estimated_T2;
        Seq.AQSlice(1).thickness=[];
   % Slice thickness in meter - [] doesn't apply any y gradient
   % Seq.AQSlice(1).Center2OriginImage=[-0.001,0.00,0.000];
       % Vector from center of the image to the origin in Image coordinate system


   % Set RF pulses
       % Rectangular RF pulse for the excitation of a wide band of frequencies in the sample
        TX.Start(1:2)   = 1e-6;
        alpha90         = pi/2;
              % alpha = gamma*B1*tau;
        alpha180        = pi;
        B1              = HW.TX.AmpMax*0.95;
        TX.Duration     = [alpha90/(gamma*B1) alpha180/(gamma*B1)];
        % TX.Duration     = [HW.tFlip90Def HW.tFlip180Def];

        TX.Frequency    = HW.fLarmor;
        TX.Phase        = [0 0];
              % Phase of 2 TX pulses
        TX.Amplitude    = B1;

        % Gradient parameters
        startGradient1 = TX.Start(1)+TX.Duration(1)+Seq.tRep(1)*1/3;
                 % Complimentary to Grad(Grad_dir).Time(3,3)
        % startGradient2 = TX.Start(1)+TX.Duration(2)+Seq.tRep(1)*1/4;
        GradTime_Factor = 2/3;
        Duration_Grad = Seq.tRep(1)*GradTime_Factor+TX.Duration(1)-
   (startGradient1+1/TX.Frequency);
        startGradient2 = Seq.tRep(1)- ( startGradient1+1/TX.Frequency + Duration_Grad +
   1/TX.Frequency ) + TX.Duration(1)/2;
```

Appendix A (continued)

```
    for k =1:3
        Grad(k).Time = [
          startGradient1
                startGradient2;
          startGradient1+1/TX.Frequency
                startGradient2+1/TX.Frequency;
        startGradient1+1/TX.Frequency + Duration_Grad
                startGradient2+1/TX.Frequency + Duration_Grad;
        startGradient1+1/TX.Frequency + Duration_Grad + 1/TX.Frequency
                startGradient2+1/TX.Frequency + Duration_Grad + 1/TX.Frequency];
    end

    Delta = Seq.tRep(1)-Grad(Grad_dir).Time(1,1)+TX.Duration(1);
    delta = Grad(Grad_dir).Time(3,1)-Grad(Grad_dir).Time(2,1);


    if Grad_dir==1      Grad(2).Amp = zeros(4,2); Grad(3).Amp = zeros(4,2);     end
    if Grad_dir==2      Grad(1).Amp = zeros(4,2); Grad(3).Amp = zeros(4,2);     end
    if Grad_dir==3      Grad(1).Amp = zeros(4,2); Grad(2).Amp = zeros(4,2);     end

    GradientAmplitude = (b_values(i)/(Delta-delta/3))^(1/2)/(gamma*delta);
    Grad(Grad_dir).Amp =  [
          0                                 0;
          GradientAmplitude                 GradientAmplitude;
          GradientAmplitude                 GradientAmplitude;
          0                                 0];
    G_max = max(Grad(Grad_dir).Amp);

    % Visualize the sequence
    Seq.plotSeq = Grad_dir;

    % Acquisition
    AQ.Start    = (TX.Start+TX.Duration+1e-4).*[1 0] + Seq.tRep(1)/2.*[0 1];
    AQ.fSample = [30e3 30e3];
    AQ.nSamples = Seq.tRep.*AQ.fSample./2.*ones(size(TX.Start));
    AQ.Frequency = HW.fLarmor.*ones(size(AQ.Start));
    AQ.Phase = 0;

    % Start measurement
    [Raw, SeqOut, data, data_1D ] = set_sequence(HW, Seq, AQ, TX, Grad);

    % Visualize acquired data
    plot_data_1D(HW, data_1D);
    clear time_all, time_all=data.time_all(:,:,:); time_all=squeeze(time_all(:));
    clear data_signal, data_signal=data.data(:,:,:);
          data_signal=squeeze(data_signal(:));

    time_all_array(i,:)     = time_all;
    data_signal_array(i,:)  = data_signal;

    if i==1
        [S0, S0_index]  = max(abs(data_signal(length(time_all)/2:length(time_all))));
        S0_index = S0_index + length(time_all)/2 - 1;
        S_interval = round(S0_index+[1+AQ.nSamples(2)/10 1-AQ.nSamples(2)/10]);
    end

    S(Grad_dir, i)      = max(abs(data_signal(S_interval(2):S_interval(1))));

    logs(Grad_dir, i)   = log(S(Grad_dir, i)/S0);
    ADC(Grad_dir, i)    = -log(S(Grad_dir, i)/S0)/b_values0(i);
    product(Grad_dir, i)= b_values0(i)*ADC(Grad_dir, i);

    % Displaying the result
    kspace = squeeze(data.data);
    imagespace = fftshift(fft2(fftshift(kspace))) .* squeeze(data.cic_corr);

    signal0 = squeeze(data.data);
    signal0(find(isnan(real(signal0))))=[];
    signal(Grad_dir,:) = signal0;
    f=linspace(-0.5*pi,0.5*pi,numel(signal(Grad_dir,:)))*AQ.fSample(1);
    % figure, plot(f,abs(fftshift(fft(signal))))

    name_i = strcat('sig_',num2str(i));
    signal_struct.(name_i) = data_1D;
end
```

Appendix A (continued)

```
    sprintf('Gradient direction: %d',Grad_dir)
    table(b_values0(Grad_dir,:), ADC(Grad_dir,:), product(Grad_dir,:))

    figure,
    tot_row = floor(n_signals/tot_col)+1;
    for i = 1:n_signals
        name_i = strcat('sig_',num2str(i));

        signal_abs(Grad_dir,:)  = abs(signal_struct.(name_i).data);
        signal_real(Grad_dir,:) = real(signal_struct.(name_i).data);
        signal_imm(Grad_dir,:)  = imag(signal_struct.(name_i).data);
        time(Grad_dir,:)        = signal_struct.(name_i).time_all;

        subplot(tot_row,tot_col,i)
        title_plot =['b_value: ' num2str(b_values0(i))];     title(title_plot, 'Interpreter',
'none' );
        y_maxvalue = max(abs(signal_struct.sig_1.data));
        hold on, grid on, ylim([-y_maxvalue-1e-9 y_maxvalue+1e-9]);
        plot(time,signal_abs, 'color',[0.91 0.41 0.17]', 'LineWidth', 3);
        plot(time,signal_real,'b', time,signal_imm,'r');
        xlabel('Time [s]'), ylabel('Amplitude [T]')
        hold off

    end
    hl = legend('abs','real','imag');
    newPosition = [0.7 0.1 0.2 0.15];
    newUnits = 'normalized';
    set(hl,'Position', newPosition,'Units', newUnits);
    ADC_plot =  b_values0\logs(Grad_dir,:)'; % m^2/s

    b_value_start = 0;
    b_value_end = 400;

    b_value_start_i = find(b_values0==b_value_start);
    b_value_end_i = find(b_values0==b_value_end);

    lm =
fitlm(b_values0(b_value_start_i:b_value_end_i),logs(Grad_dir,(b_value_start_i:b_value_end_i))'
);

    figure, plot(b_values0,logs(Grad_dir,:)','b*'), xlabel('b value'), ylabel('ln(S0/S)'), hold
on, grid on,
    plot(b_values0(b_value_end_i),logs(Grad_dir,b_value_end_i)','*','LineWidth',3),
    plot(b_values0(b_value_start_i),logs(Grad_dir,b_value_start_i)','*','LineWidth',3),


plot(b_values0(b_value_start_i:b_value_end_i),table2array(lm.Coefficients(1,1))+table2array(lm
.Coefficients(2,1)).*b_values0(b_value_start_i:b_value_end_i),'r--')
    D_value_i = table2array(lm.Coefficients(2,1));

    titleplot = strcat('Plot for Gradient Direction ',num2str(Grad_dir));
    title(titleplot);

    format long
    D_value(Grad_dir) = - 1000*D_value_i
    format short

    Sample_number = num2str(Num_sample);
    name_file = strcat('Diffusion',Substance,Sample_number,'_Dir',num2str(Grad_dir),'_3000');

    pause(10);
end

D_value
load handel.mat
sound(y)

%%
% by Marco Andrea Zampini, March 2018
```

Appendix B

AUTHORIZATIONS

Appendix B (continued)

JOHN WILEY AND SONS LICENSE TERMS AND CONDITIONS

Apr 20, 2018

This Agreement between Marco Andrea Zampini ("You") and John Wiley and Sons ("John Wiley and Sons") consists of your license details and the terms and conditions provided by John Wiley and Sons and Copyright Clearance Center.

License Number	4330360888714
License date	Apr 15, 2018
Licensed Content Publisher	John Wiley and Sons
Licensed Content Publication	Contrast Media & Molecular Imaging
Licensed Content Title	Comparative study of the physicochemical properties of six clinical low molecular weight gadolinium contrast agents
Licensed Content Author	Sophie Laurent, Luce Vander Elst, Robert N. Muller
Licensed Content Date	Jun 22, 2006
Licensed Content Volume	1
Licensed Content Issue	3
Licensed Content Pages	10
Type of use	Dissertation/Thesis
Requestor type	University/Academic
Format	Electronic
Portion	Figure/table
Number of figures/tables	2
Original Wiley figure/table number(s)	Figure 2 and Figure 4
Will you be translating?	No
Title of your thesis / dissertation	0.5T Benchtop Magnet: Development of a MR Elastography Setup and Tissue Samples Characterization
Expected completion date	May 2018
Expected size (number of pages)	120
Requestor Location	Marco Andrea Zampini 1910 North Mozart Street CHICAGO, IL 60647 United States Attn: Marco Andrea Zampini
Publisher Tax ID	EU826007151
Total	0.00 USD
Terms and Conditions	

TERMS AND CONDITIONS

This copyrighted material is owned by or exclusively licensed to John Wiley & Sons, Inc. or one of its group companies (each a"Wiley Company") or handled on behalf of a society with which a Wiley Company has exclusive publishing rights in relation to a particular work

Appendix B (continued)

(collectively "WILEY"). By clicking "accept" in connection with completing this licensing transaction, you agree that the following terms and conditions apply to this transaction (along with the billing and payment terms and conditions established by the Copyright Clearance Center Inc., ("CCC's Billing and Payment terms and conditions"), at the time that you opened your RightsLink account (these are available at any time at http://myaccount.copyright.com).

Terms and Conditions

- The materials you have requested permission to reproduce or reuse (the "Wiley Materials") are protected by copyright.

- You are hereby granted a personal, non-exclusive, non-sub licensable (on a stand-alone basis), non-transferable, worldwide, limited license to reproduce the Wiley Materials for the purpose specified in the licensing process. This license, **and any CONTENT (PDF or image file) purchased as part of your order,** is for a one-time use only and limited to any maximum distribution number specified in the license. The first instance of republication or reuse granted by this license must be completed within two years of the date of the grant of this license (although copies prepared before the end date may be distributed thereafter). The Wiley Materials shall not be used in any other manner or for any other purpose, beyond what is granted in the license. Permission is granted subject to an appropriate acknowledgement given to the author, title of the material/book/journal and the publisher. You shall also duplicate the copyright notice that appears in the Wiley publication in your use of the Wiley Material. Permission is also granted on the understanding that nowhere in the text is a previously published source acknowledged for all or part of this Wiley Material. Any third party content is expressly excluded from this permission.

- With respect to the Wiley Materials, all rights are reserved. Except as expressly granted by the terms of the license, no part of the Wiley Materials may be copied, modified, adapted (except for minor reformatting required by the new Publication), translated, reproduced, transferred or distributed, in any form or by any means, and no derivative works may be made based on the Wiley Materials without the prior permission of the respective copyright owner.**For STM Signatory Publishers clearing permission under the terms of the STM Permissions Guidelines only, the terms of the license are extended to include subsequent editions and for editions in other languages, provided such editions are for the work as a whole in situ and does not involve the separate exploitation of the permitted figures or extracts,** You may not alter, remove or suppress in any manner any copyright, trademark or other notices displayed by the Wiley Materials. You may not license, rent, sell, loan, lease, pledge, offer as security, transfer or assign the Wiley Materials on a stand-alone basis, or any of the rights granted to you hereunder to any other person.

- The Wiley Materials and all of the intellectual property rights therein shall at all times remain the exclusive property of John Wiley & Sons Inc, the Wiley Companies, or their respective licensors, and your interest therein is only that of having possession of and the right to reproduce the Wiley Materials pursuant to Section 2 herein during the continuance of this Agreement. You agree that you own no right, title or interest in or to the Wiley Materials or any of the intellectual property rights therein. You shall have no rights hereunder other than the license as provided for above in Section 2. No right, license or interest to any trademark, trade name, service mark or other branding ("Marks") of WILEY or its licensors is granted hereunder, and you agree that you shall not assert any such right, license or interest with respect thereto

Appendix B (continued)

- NEITHER WILEY NOR ITS LICENSORS MAKES ANY WARRANTY OR REPRESENTATION OF ANY KIND TO YOU OR ANY THIRD PARTY, EXPRESS, IMPLIED OR STATUTORY, WITH RESPECT TO THE MATERIALS OR THE ACCURACY OF ANY INFORMATION CONTAINED IN THE MATERIALS, INCLUDING, WITHOUT LIMITATION, ANY IMPLIED WARRANTY OF MERCHANTABILITY, ACCURACY, SATISFACTORY QUALITY, FITNESS FOR A PARTICULAR PURPOSE, USABILITY, INTEGRATION OR NON-INFRINGEMENT AND ALL SUCH WARRANTIES ARE HEREBY EXCLUDED BY WILEY AND ITS LICENSORS AND WAIVED BY YOU.

- WILEY shall have the right to terminate this Agreement immediately upon breach of this Agreement by you.

- You shall indemnify, defend and hold harmless WILEY, its Licensors and their respective directors, officers, agents and employees, from and against any actual or threatened claims, demands, causes of action or proceedings arising from any breach of this Agreement by you.

- IN NO EVENT SHALL WILEY OR ITS LICENSORS BE LIABLE TO YOU OR ANY OTHER PARTY OR ANY OTHER PERSON OR ENTITY FOR ANY SPECIAL, CONSEQUENTIAL, INCIDENTAL, INDIRECT, EXEMPLARY OR PUNITIVE DAMAGES, HOWEVER CAUSED, ARISING OUT OF OR IN CONNECTION WITH THE DOWNLOADING, PROVISIONING, VIEWING OR USE OF THE MATERIALS REGARDLESS OF THE FORM OF ACTION, WHETHER FOR BREACH OF CONTRACT, BREACH OF WARRANTY, TORT, NEGLIGENCE, INFRINGEMENT OR OTHERWISE (INCLUDING, WITHOUT LIMITATION, DAMAGES BASED ON LOSS OF PROFITS, DATA, FILES, USE, BUSINESS OPPORTUNITY OR CLAIMS OF THIRD PARTIES), AND WHETHER OR NOT THE PARTY HAS BEEN ADVISED OF THE POSSIBILITY OF SUCH DAMAGES. THIS LIMITATION SHALL APPLY NOTWITHSTANDING ANY FAILURE OF ESSENTIAL PURPOSE OF ANY LIMITED REMEDY PROVIDED HEREIN.

- Should any provision of this Agreement be held by a court of competent jurisdiction to be illegal, invalid, or unenforceable, that provision shall be deemed amended to achieve as nearly as possible the same economic effect as the original provision, and the legality, validity and enforceability of the remaining provisions of this Agreement shall not be affected or impaired thereby.

- The failure of either party to enforce any term or condition of this Agreement shall not constitute a waiver of either party's right to enforce each and every term and condition of this Agreement. No breach under this agreement shall be deemed waived or excused by either party unless such waiver or consent is in writing signed by the party granting such waiver or consent. The waiver by or consent of a party to a breach of any provision of this Agreement shall not operate or be construed as a waiver of or consent to any other or subsequent breach by such other party.

- This Agreement may not be assigned (including by operation of law or otherwise) by you without WILEY's prior written consent.

- Any fee required for this permission shall be non-refundable after thirty (30) days from receipt by the CCC.

Appendix B (continued)

- These terms and conditions together with CCC's Billing and Payment terms and conditions (which are incorporated herein) form the entire agreement between you and WILEY concerning this licensing transaction and (in the absence of fraud) supersedes all prior agreements and representations of the parties, oral or written. This Agreement may not be amended except in writing signed by both parties. This Agreement shall be binding upon and inure to the benefit of the parties' successors, legal representatives, and authorized assigns.

- In the event of any conflict between your obligations established by these terms and conditions and those established by CCC's Billing and Payment terms and conditions, these terms and conditions shall prevail.

- WILEY expressly reserves all rights not specifically granted in the combination of (i) the license details provided by you and accepted in the course of this licensing transaction, (ii) these terms and conditions and (iii) CCC's Billing and Payment terms and conditions.

- This Agreement will be void if the Type of Use, Format, Circulation, or Requestor Type was misrepresented during the licensing process.

- This Agreement shall be governed by and construed in accordance with the laws of the State of New York, USA, without regards to such state's conflict of law rules. Any legal action, suit or proceeding arising out of or relating to these Terms and Conditions or the breach thereof shall be instituted in a court of competent jurisdiction in New York County in the State of New York in the United States of America and each party hereby consents and submits to the personal jurisdiction of such court, waives any objection to venue in such court and consents to service of process by registered or certified mail, return receipt requested, at the last known address of such party.

WILEY OPEN ACCESS TERMS AND CONDITIONS

Wiley Publishes Open Access Articles in fully Open Access Journals and in Subscription journals offering Online Open. Although most of the fully Open Access journals publish open access articles under the terms of the Creative Commons Attribution (CC BY) License only, the subscription journals and a few of the Open Access Journals offer a choice of Creative Commons Licenses. The license type is clearly identified on the article.

The Creative Commons Attribution License

The Creative Commons Attribution License (CC-BY) allows users to copy, distribute and transmit an article, adapt the article and make commercial use of the article. The CC-BY license permits commercial and non-

Creative Commons Attribution Non-Commercial License

The Creative Commons Attribution Non-Commercial (CC-BY-NC)License permits use, distribution and reproduction in any medium, provided the original work is properly cited and is not used for commercial purposes.(see below)

Creative Commons Attribution-Non-Commercial-NoDerivs License

The Creative Commons Attribution Non-Commercial-NoDerivs License (CC-BY-NC-ND) permits use, distribution and reproduction in any medium, provided the original work is properly cited, is not used for commercial purposes and no modifications or adaptations are made. (see below)

Use by commercial "for-profit" organizations

Use of Wiley Open Access articles for commercial, promotional, or marketing purposes requires further explicit permission from Wiley and will be subject to a fee.

Appendix B (continued)

Further details can be found on Wiley Online Library
http://olabout.wiley.com/WileyCDA/Section/id-410895.html

Other Terms and Conditions:

v1.10 Last updated September 2015

Questions? customercare@copyright.com or +1-855-239-3415 (toll free in the US) or +1-978-646-2777.

CITED LITERATURE

1. Shokrollahi, H.: Contrast agents for mri. Materials Science and Engineering: C, 33(8):4485 – 4497, 2013.

2. Bernstein, M., King, K., and Zhou, X.: Introduction to radiofrequency pulses. In Handbook of {MRI} Pulse Sequences, eds. M. Bernstein, K. King, and X. Zhou, pages 29 – 34. Burlington, Academic Press, 2004.

3. Hendrick, E. et al.: Glossary of mr terms. Accessed: 2018-02-20.

4. Liang, Z.-P. and Lauterbur, P. C.: Principles of magnetic resonance imaging: a signal processing perspective. SPIE Optical Engineering Press, 2000.

5. Bernstein, M., King, K., and Zhou, X.: Chapter 7 - gradient lobe shapes. In Handbook of {MRI} Pulse Sequences, eds. M. Bernstein, K. King, and X. Zhou, pages 219 – 242. Burlington, Academic Press, 2004.

6. Bernstein, M., King, K., and Zhou, X.: Chapter 9 - motion-sensitizing gradients. In Handbook of {MRI} Pulse Sequences, eds. M. Bernstein, K. King, and X. Zhou, pages 274 – 291. Burlington, Academic Press, 2004.

7. Qin, E. C., Sinkus, R., Geng, G., Cheng, S., Green, M., Rae, C. D., and Bilston, L. E.: Combining mr elastography and diffusion tensor imaging for the assessment of anisotropic mechanical properties: A phantom study. Journal of Magnetic Resonance Imaging, 37(1):217–226.

8. Ipek-Ugay, S., Driele, T., Ledwig, M., Guo, J., Hirsch, S., Sack, I., and Braun, J.: Tabletop magnetic resonance elastography for the measurement of viscoelastic parameters of small tissue samples. Journal of Magnetic Resonance, 251:13 – 18, 2015.

9. Glaser, K. J., Manduca, A., and Ehman, R. L.: Review of mr elastography applications and recent developments. Journal of Magnetic Resonance Imaging, 36(4):757–774, 2012.

CITED LITERATURE (continued)

10. Klatt, D., Friedrich, C., Korth, Y., Vogt, R., Braun, J., and Sack, I.: Viscoelastic properties of liver measured by oscillatory rheometry and multifrequency magnetic resonance elastography. Biorheology, 47(2):133–141, 8 2010.

11. Fung, Y.: Biomechanics - Mechanical Properties of Living Tissues. Springer, 1981.

12. Doyley, M.: Model-based elastography: a survey of approaches to the inverse elasticity problem. Physics in Medicine & Biology, 57(3):R35, 2012.

13. Schmidt, J., Tweten, D., Badachhape, A., Reiter, A., Okamoto, R., Garbow, J., and Bayly, P.: Measurement of anisotropic mechanical properties in porcine brain white matter ex vivo using magnetic resonance elastography. Journal of the mechanical behavior of biomedical materials, 79:30–37, 2018.

14. Venkatesh, S. K. and Ehman, R. L.: Magnetic resonance elastography. Springer, 2014.

15. Morrow, D. A., Donahue, T. L. H., Odegard, G. M., and Kaufman, K. R.: Transversely isotropic tensile material properties of skeletal muscle tissue. Journal of the mechanical behavior of biomedical materials, 3(1):124–129, 2010.

16. Chui, C., Kobayashi, E., Chen, X., Hisada, T., and Sakuma, I.: Transversely isotropic properties of porcine liver tissue: experiments and constitutive modelling. Medical & biological engineering & computing, 45(1):99–106, 2007.

17. Girometti, R., Esposito, G., Bagatto, D., Avellini, C., Bazzocchi, M., and Zuiani, C.: Is water diffusion isotropic in the cirrhotic liver? a study with diffusion-weighted imaging at 3.0 tesla. Academic radiology, 19(1):55–61, 2012.

18. Chilla, G. S., Tan, C. H., Xu, C., and Poh, C. L.: Diffusion weighted magnetic resonance imaging and its recent trenda survey. Quantitative Imaging in Medicine and Surgery, 5(3), 2015.

19. Goss, W., Matthews, H., and Winnberg, A.: High-resolution observations of the w33 complex at 2.8, 6, 18 and 21 cm. Astronomy and Astrophysics, 65:307–312, 1978.

20. Liver histology. `https://www.kenhub.com/en/library/anatomy/liver-histology`. Accessed: 2018-04-12.

21. Nuclear magnetic relaxation dispersion (nmrd) profile. `http://histologylab.ccnmtl.columbia.edu/lab17/liver.html`. Accessed: 2018-03-12.

CITED LITERATURE (continued)

22. Taouli, B., Vilgrain, V., Dumont, E., Daire, J.-L., Fan, B., and Menu, Y.: Evaluation of liver diffusion isotropy and characterization of focal hepatic lesions with two single-shot echo-planar mr imaging sequences: prospective study in 66 patients. Radiology, 226(1):71–78, 2003.

23. Rooney, W. D., Johnson, G., Li, X., Cohen, E. R., Kim, S.-G., Ugurbil, K., and Springer, C. S.: Magnetic field and tissue dependencies of human brain longitudinal 1h2o relaxation in vivo. Magnetic Resonance in Medicine, 57(2):308–318, 2007.

24. Diffusion tensor. `http://mriquestions.com/diffusion-tensor.html`. Accessed: 2018-04-08.

25. Vappou, J., Breton, E., Choquet, P., Willinger, R., and Constantinesco, A.: Assessment of in vivo and post-mortem mechanical behavior of brain tissue using magnetic resonance elastography. Journal of biomechanics, 41(14):2954–2959, 2008.

26. Bloch, F.: Nuclear induction. Phys. Rev., 70:460–474, Oct 1946.

27. Rohrer, M., Bauer, H., Mintorovitch, J., Requardt, M., and Weinmann, H.-J.: Comparison of magnetic properties of mri contrast media solutions at different magnetic field strengths. Investigative Radiology, 40(11), 2005.

28. Kraft, K. A., Fatouros, P. P., Clarke, G. D., and Kishore, P. R. S.: An mri phantom material for quantitative relaxometry. Magnetic Resonance in Medicine, 5(6):555–562.

29. Laurent, S., Elst, L. V., and Muller, R. N.: Comparative study of the physicochemical properties of six clinical low molecular weight gadolinium contrast agents. Contrast Media & Molecular Imaging, 1(3):128–137.

30. Carneiro, A. A. O., Vilela, G. R., Araujo, D. B. d., and Baffa, O.: MRI relaxometry: methods and applications. Brazilian Journal of Physics, 36:9 – 15, 03 2006.

31. Kato, H., Kuroda, M., Yoshimura, K., Yoshida, A., Hanamoto, K., Kawasaki, S., Shibuya, K., and Kanazawa, S.: Composition of mri phantom equivalent to human tissues. Medical physics, 32(10):3199–3208, 2005.

32. Nuclear magnetic relaxation dispersion (nmrd) profile. `http://www.invento-lab.com/NMRD.html`. Accessed: 2018-03-25.

CITED LITERATURE (continued)

33. Uggeri, F., Aime, S., Anelli, P. L., Botta, M., Brocchetta, M., de Haeen, C., Ermondi, G., Grandi, M., and Paoli, P.: Novel contrast agents for magnetic resonance imaging. synthesis and characterization of the ligand bopta and its ln (iii) complexes (ln= gd, la, lu). x-ray structure of disodium (tps-9-145337286-cs)-[4-carboxy-5, 8, 11-tris (carboxymethyl)-1-phenyl-2-oxa-5, 8, 11-triazatridecan-13-oato (5-)] gadolinate (2-) in a mixture with its enantiomer. Inorganic Chemistry, 34(3):633–643, 1995.

34. Pintaske, J., Martirosian, P., Graf, H., Erb, G., Lodemann, K.-P., Claussen, C., and Schick, F.: Relaxivity of gadopentetate dimeglumine (magnevist), gadobutrol (gadovist), and gadobenate dimeglumine (multihance) in human blood plasma at 0.2, 1.5, and 3 tesla. 41:213–21, 04 2006.

35. Multihance. `https://imaging.bracco.com/us-en/products/magnetic-resonance-imaging/multihance`. Accessed: 2018-02-17.

36. Diakova, G., Korb, J., and Bryant, R.: The magnetic field dependence of water t(1) in tissues. Magnetic Resonance in Medicine, 68(1):272–277, 07 2012.

37. Korb, J. and Bryant, R.: Magnetic field dependence of proton spin-lattice relaxation times. Magnetic Resonance in Medicine, 48(1):21–26, 2002.

38. Bottomley, P. A., Foster, T. H., Argersinger, R. E., and Pfeifer, L. M.: A review of normal tissue hydrogen nmr relaxation times and relaxation mechanisms from 1100 mhz: Dependence on tissue type, nmr frequency, temperature, species, excision, and age. Medical Physics, 11(4):425–448.

39. Stejskal, E. O. and Tanner, J. E.: Spin diffusion measurements: Spin echoes in the presence of a timedependent field gradient. The Journal of Chemical Physics, 42(1):288–292, 1965.

40. Bihan, D. L., Breton, E., Lallemand, D., Grenier, P., Cabanis, E., and Laval-Jeantet, M.: Mr imaging of intravoxel incoherent motions: application to diffusion and perfusion in neurologic disorders. Radiology, 161(2):401–407, 1986. PMID: 3763909.

41. Eghtedari, M., Ma, J., Fox, P., Guvenc, I., Yang, W. T., and Dogan, B. E.: Effects of magnetic field strength and b value on the sensitivity and specificity of quantitative breast diffusion-weighted mri. Quantitative Imaging in Medicine and Surgery, 6(4), 2016.

CITED LITERATURE (continued)

42. Tsien, C., Cao, Y., and Chenevert, T.: Clinical applications for diffusion magnetic resonance imaging in radiotherapy. Seminars in Radiation Oncology, 24(3):218–226, 2018/04/07.

43. Iima, M. and Le Bihan, D.: Clinical intravoxel incoherent motion and diffusion mr imaging: past, present, and future. Radiology, 278(1):13–32, 2015.

44. Cleveland, G., Chang, D., Hazlewood, C., and Rorschach, H.: Nuclear magnetic resonance measurement of skeletal muscle: anisotrophy of the diffusion coefficient of the intracellular water. Biophysical Journal, 16(9):1043 – 1053, 1976.

45. Damon, B. M., Buck, A. K., and Ding, Z.: Diffusion-tensor mri based skeletal muscle fiber tracking. Imaging in medicine, 3(6):675, 2011.

46. Mukherjee, P., Berman, J., Chung, S., Hess, C., and Henry, R.: Diffusion tensor mr imaging and fiber tractography: theoretic underpinnings. American journal of neuroradiology, 29(4):632–641, 2008.

47. Schwenzer, N. F., Steidle, G., Martirosian, P., Schraml, C., Springer, F., Claussen, C. D., and Schick, F.: Diffusion tensor imaging of the human calf muscle: distinct changes in fractional anisotropy and mean diffusion due to passive muscle shortening and stretching. NMR in biomedicine, 22(10):1047–1053, 2009.

48. Linear viscoelasticity. `http://www.ucl.ac.uk/~ucahhwi/GM05/lecture3.pdf`. Accessed: 2018-04-10.

49. Venkatesh, S. K. and Ehman, R. L.: Magnetic resonance elastography of liver. Magnetic Resonance Imaging Clinics, 22(3):433–446, 2014.

50. Manduca, A., Oliphant, T. E., Dresner, M. A., Mahowald, J. L., Kruse, S. A., Amromin, E., Felmlee, J. P., Greenleaf, J. F., and Ehman, R. L.: Magnetic resonance elastography: Non-invasive mapping of tissue elasticity. Medical Image Analysis, 5(4):237–254, 2018/04/09.

51. Yasar, T. K., Royston, T. J., and Magin, R. L.: Wideband mr elastography for viscoelasticity model identification. Magnetic resonance in medicine, 70(2):479–489, 2013.

52. Riek, K., Klatt, D., Nuzha, H., Mueller, S., Neumann, U., Sack, I., and Braun, J.: Wide-range dynamic magnetic resonance elastography. Journal of Biomechanics, 44(7):1380–1386, 2011.

CITED LITERATURE (continued)

53. Braun, J., Tzschätzsch, H., Körting, C., Ariza de Schellenberger, A., Jenderka, M., Drießle, T., Ledwig, M., and Sack, I.: A compact 0.5 t mr elastography device and its application for studying viscoelasticity changes in biological tissues during progressive formalin fixation. Magnetic resonance in medicine, 79(1):470–478, 2018.

54. Tuning and matching. `http://www.nmr2.buffalo.edu/nesg.wiki/Tuning_and_matching`. Accessed: 2018-04-05.

55. High load stack type series pahl - pahl 60/20 datasheet. `https://www.piezosystem.com/products/piezo_actuators/stacktypeactuators/series_pahl/`. Accessed: 2018-03-01.

56. Dale, B. M., Brown, M. A., and Semelka, R. C.: MRI: basic principles and applications. John Wiley & Sons, 2015.

57. Ghiglia, D. C. and Pritt, M. D.: Two-dimensional phase unwrapping: theory, algorithms, and software, volume 4. Wiley New York, 1998.

58. Chapter 10 - correction gradients, editor =.

59. Alexander, A. L., Lee, J. E., Lazar, M., and Field, A. S.: Diffusion tensor imaging of the brain. Neurotherapeutics, 4(3):316–329, 2007.

60. Nath, K., Saraswat, V. A., Krishna, Y. R., Thomas, M. A., Rathore, R. K., Pandey, C. M., and Gupta, R. K.: Quantification of cerebral edema on diffusion tensor imaging in acute-on-chronic liver failure. NMR in biomedicine, 21(7):713–722, 2008.

61. Bernstein, M., King, K., and Zhou, X.: Handbook of MRI Pulse Sequences. Elsevier Academic Press, 2004.

VITA

NAME	Marco Andrea Zampini
EDUCATION	
Aug 2018	Master of Science in Bioengineering, University of Illinois at Chicago, USA
Exp. Dec 2018	Master Degree in Bioengineering, Politecnico di Milano, Italy - focus on the Electronic Technologies track. Major classes: Biomedical Electronics, Biomedical Signal and Image Processing, Medical Applications of Radiation Fields, Methods for Biomedical Imaging and Computer Aided Surgery, Technologies for Sensors and Clinical Instrumentation, Haptics, Bioengineering of Neurosensory and Physiological Control Systems, Patents and Intellectual Property
Jul 2016	Bachelor of Science in Biomedical Engineering, Politecnico di Milano, Italy
LANGUAGE SKILLS	
Italian	Native speaker
English	Full working proficiency
A.Y. 2017/18	Double degree program abroad in Chicago, Illinois
A.Y. 2016/18	Lessons and exams attended exclusively in English
May 2016	TOEFL examination (101/120)
SCHOLARSHIPS	
Spring 2018	Graduate Research Assistantship (RA) position (20 hours/week) with full tuition waiver and monthly stipend
A.Y. 2017/18	Italian scholarship for excellent students at Politecnico di Milano
A.Y. 2016/17	Italian scholarship for excellent students at Politecnico di Milano
TECHNICAL SKILLS	
Average level	R, Arduino, VolView, Paraview, ITK-SNAP, Quick Haptics, HTML, JAVA, Phyton
Advanced level	MATLAB, Processing, SolidWorks, C, C++

VITA (continued)

WORK EXPERIENCE AND PROJECTS

May 2017	Development of a project called “HelloPlants!”, an Arduino-Processing application for plants homecare based on Twitter updates and a light intensity monitoring through a LDR sensor
Jul 2016	Thesis project ”A visual-biofeedback guided randomized controlled trial to assess the balance in post-acute stroke patients following a balance board training” at Politecnico di Milano in collaboration with Foundazione Maugeri